Boundary-condition models of film-cooling holes for large-eddy simulation of turbine vanes

Dorian Dupuy, Aurélien Perrot, Nicolas Odier, Laurent Y. M. Gicquel, Florent Duchaine

Boundary-condition models of film-cooling holes for large-eddy simulation of turbine vanes

Dorian Dupuy*[1], Aurélien Perrot[1,2], Nicolas Odier[1], Laurent Gicquel[1], and Florent Duchaine[1]

[1] *European Centre for Research and Advanced Training in Scientific Computing, Toulouse F-31057 Cedex 1, France*

[2] *Safran Helicopter Engines, Avenue Joseph Szydlowski, Bordes, France*

(Published version: International Journal of Heat and Mass Transfer 166, 120763 (2021); https://doi.org/10.1016/j.ijheatmasstransfer.2020.120763)

Abstract

In many industrial applications, the mechanical integrity of a surface operating under large thermal loads is ensured by injecting a cold fluid through a series of hole along the surface, forming a thin film of cool fluid shielding the solid surface from external heat. An accurate prediction of the heat transfer provided by these so-called film-cooling systems is crucial to ensure the durability of the cooled surfaces. However, the large-eddy simulation of film-cooling systems is complex and expensive because the in-hole flow must be meshed and simulated. To address this difficulty, the modelling of the film-cooling jet by mean of a dedicated boundary condition has recently been proposed. This paper investigates several potential improvements for this type of model in four geometries: an inclined cylindrical hole, a fanshaped hole and two fanshaped laidback holes. The analysis focuses on the comparison of a spatially uniform injection to a model taking into account velocity and temperature spatial variations at the hole exit. The study also compares a non-turbulent injection to a model with synthetic turbulence injection. The comparisons are first performed using a fine mesh to validate the approach, then using a coarse mesh representative of a mesh that could be used to simulate a cooled nozzle guide vane. The results show that both spatial inhomogeneity and turbulence injection significantly improve the cooling effectiveness predictions in a wide variety of cases. The spatial inhomogeneity is especially crucial for the near-hole behaviour of the flow while turbulence injection is particularly important when the destabilisation of the jet by the crossflow is not sufficient to immediately trigger transition. Using a very coarse mesh, the turbulent mixing is observed to be underestimated with all examined boundary-condition models and the behaviour of the jet is not correctly described for some of the configurations investigated. Although not sufficient, non-negligible improvements are nevertheless obtained with an inhomogeneous turbulent injection compared to the baseline uniform model.

1 Introduction

Turbomachineries, devices that transfer energy between a rotor and a fluid, are used in many industrial applications, including power generation and aircraft propulsion. In both cases, high operating temperatures must be used to maximize the thermodynamic efficiency of the system. Specific cooling systems must therefore be used to ensure that temperatures that are above the melting point of the materials used do not destroy the components. Many cooling systems have been proposed in the literature, such as transpiration cooling [19], effusion cooling [39] or film cooling [26, 9]. Film cooling technologies protect the mechanical integrity of a surface exposed to a large thermomechanical load by injecting a cooler fluid through one or more holes along the surface. These film-cooling jets are closely related to the jet-in-crossflow academic configuration [47, 69, 51, 46] with the specificity that film cooling places particular emphasis on the attachment of the jet to the wall surface. Film-cooling jets are thus generally inclined with respect to the main crossflow, which affects the jet penetration and its interaction with the crossflow [6, 7].

*Corresponding author : dorian.dupuy@cerfacs.fr

Nomenclature

BR	Blowing ratio, $\rho_h U_h / (\rho_\infty U_\infty)$
C	Concordance correlation coefficient
C_p	Heat capacity at constant pressure
c	Speed of sound
D	Hole diameter
DR	Density ratio, ρ_h / ρ_∞
E	Total energy per unit mass
H	Total enthalpy per unit mass
IQ_ν	Celik's viscous index of resolution quality
k	Turbulence kinetic energy per unit mass
Ma	Mach number
P	Pressure, or lateral distance between holes
P_s	Stagnation pressure
Pr	Prandtl number
$\boldsymbol{Q}$	Conductive heat flux
Q	Q criterion
Re	Reynolds number
$\boldsymbol{r}$	Position vector
$\mathcal{S}$	Streamline
$\overline{\mathcal{S}}$	Mean streamline
$\mathbf{S}$	Rate of deformation tensor
T	Temperature
T_s	Stagnation temperature
t	Time
$\boldsymbol{U}$	Velocity vector
U_τ	Friction velocity
u	Velocity component
x	Streamwise coordinate
y	Plate-normal coordinate
z	Spanwise coordinate
α	Injection angle
γ	Compound angle
θ	Adiabatic effectiveness, $(T_\infty - T)/(T_\infty - T_h)$
λ	Thermal conductivity
μ	Dynamic viscosity
ν	Kinematic viscosity
$\boldsymbol{\sigma}$	Shear-stress tensor
$\langle\cdot\rangle$	Statistical average
$\cdot'$	Fluctuation with respect to $\langle\cdot\rangle$

Subscripts and superscripts

d	Deviatoric part
H	Hole exit
HU	Hole-exit uniform
h	Hole
mesh	Hole-meshed computation
mod	Hole-modelled computation
$\mathcal{P}$	Plate, bottom boundary of the crossflow channel
sgs	Subgrid scale
$\mathcal{V}$	Volume of the domain
∞	Freestream
$+$	Wall-unit scaling

Abbreviations and acronyms

CRVP	Counter-rotating vortex pair
FTT	Flow-through time
GFS	Gritsch fanshaped hole
GFS	Gritsch's fanshaped hole
GLBFS	Gritsch laidback fanshaped hole
InC	Front boundary of the crossflow channel
InP	Bottom boundary of the plenum
NI	Non-uniform injection
Ou	Rear boundary of the crossflow channel
RANS	Reynolds-averaged Navier–Stokes
S&T777	Schroeder & Thole 7-7-7 hole
Sym	Symmetric boundary condition
TNI	Turbulent non-uniform injection
TUI	Turbulent uniform injection
Top	Top boundary of the crossflow channel
UI	Uniform injection
WALE	Wall-adapting local eddy-viscosity
WCT	Wall-clock time

Indeed, vortical structures generated at the exit of the film-cooling holes have a negative impact on the cooling performance since they increase the mixing of hot and cold fluid [36]. Structures such as the jet shear-layer vortices, horseshoe vortices or the counter-rotating vortex pair (CRVP) have been identified as being caused by the interaction between the crossflow and the inclined jet [21, 22, 35, 61] but are also influenced by vortices in the in-hole flow [2]. Shaped film-cooling holes have a non-cylindrical shape intended to improve the cooling performance of the jet [12]. A wide variety of shaped film-cooling hole geometries have been suggested in the literature, including fanshaped, laidback, fanshaped laidback, conical or console holes [27, 62, 63, 32, 41, 40, 66]. In particular, film-cooling holes with an expanded exit have been found to reduce the CRVP for a given blowing ratio and diameter due to a lower jet velocity [73, 77] and prevent in-hole vortices from escaping to the crossflow [1]. Film-cooling jets with a compound angle have also a modified interaction with the crossflow which can inhibit the formation of the CRVP, positively impacting the cooling performance for both cylindrical [64, 67, 44, 43] and shaped holes [10, 30, 31, 74].

The consequence of these observations is that numerical simulations of film-cooling configurations should properly represent the interaction between the crossflow and the inclined jet to accurately predict cooling performances. Reynolds-averaged Navier–Stokes (RANS) models have shown mixed results as they tend to underestimate the mixing and lateral spreading of the jet [37, 33, 79, 78, 20]. A more accurate description of the flow physics and of the cooling performances is provided by more expensive numerical procedures such as direct numerical simulation [50, 51, 23] or large-eddy simulation [75, 28, 57, 34, 61, 80, 55, 56, 2, 1, 74]. However, large-eddy simulation of film cooling is usually associated with a relatively large numerical cost that precludes its use outside of academic configurations. Indeed, the large-eddy simulation of industrial cooled high-pressure turbines is a considerable challenge as the geometry is complex and may involve hundreds of cooling holes on each blade. In such configurations, the requirement to mesh and simulate each cooling hole in addition to the main flow leads to prohibitive numerical costs. The modelling of the cooling system removes this constraint, improving the convenience of the mesh creation process, reducing the size of the computational domain and allowing the use of coarser meshes. Several modelling approaches have been proposed in the literature, including local mass-source models [5, 76, 4], distributed mass-source models [3] or the imprinting models of Rida *et al.* [59], Briones *et al.* [11]. The modelling of the jet as a boundary condition has also been developed in the context of the effusion cooling systems found on the multiperforated plates of combustion chambers. In that context, Mendez and Nicoud [49] suggested the modelling of the jets by a homogeneous injection of cold fluid over the wall surface that preserves the mass and momentum fluxes of the jets. To capture the position and individual dynamics of the jets, Bizzari *et al.* [8] then proposed the thickened-hole model that takes into account the local mesh refinement around the holes. Harnieh *et al.* [29] finally examined the applicability of this boundary-condition model to the numerical simulation of a cooled nozzle guide vane. In this last case, the film-cooling wall model is found to provide insufficient level of turbulence kinetic energy and turbulent mixing between the cold fluid and the main flow.

This paper investigates several potential improvements for boundary-condition film-cooling models and focuses in particular on the addition of spatial inhomogeneity and synthetic turbulence injection to reproduce the in-hole agitation. For this purpose, different jet-in-crossflow configurations on a flat plate without freestream turbulence and at low Mach number are considered. To ensure the generalisability of the models to the wide variety of possible film-cooling hole geometries for turbine-blade design, the analysis is performed for four hole geometries: an inclined cylindrical hole, the fanshaped and fanshaped laidback hole of Gritsch *et al.* [27] and the fanshaped laidback hole of Schroeder and Thole [66]. In addition, the relevance of the type of model to be used is assessed for several blowing ratios and compound angles to address the robustness of the models to variations of operating conditions, which is crucial as each film-cooling hole in a turbine blade may experience different flow conditions. In total, 12 flow configurations are investigated. For each flow configuration, a reference large-eddy simulation in which the in-hole flow and the plenum are simulated is first performed using a finite-element method in a cell-vertex formulation and a two-step Taylor–Galerkin scheme [15]. Four simulations with a jet boundary-condition model are then carried out using the same numerical method and mesh refinement as for the reference simulation and using the reference simulation to inform the spatial inhomogeneity and turbulence level at the

Table 1: Geometric parameters of the film-cooling holes. Refer to figure 1 for notations.

Geometry	L_1/D	L_2/D	L_m/D	L_f/D	L_w/D	L_ℓ/D	α	β_f	β_ℓ
Cylinder	2.0	1.0	6.0	—	6.0	—	30°	—	—
GFS [27]	2.0	3.1	6.0	—	2.0	4.0	30°	—	14°
GLBFS [27]	3.9	3.5	5.0	1.0	2.0	4.0	30°	15°	14°
S&T777 [66]	3.4	2.1	2.5	3.5	2.5	3.5	30°	7°	7°

exit of the film-cooling hole. Finally, four additional simulations with a coarser mesh are performed in order to study the effect of mesh coarsening on the hole-modelled simulations, in particular with regard to the level of turbulence downstream of the jet and the cooling performances.

The paper is organised as follows. The flow configurations and the numerical procedure are presented in section 2. The results are analysed and discussed in section 3.

2 Flow Configurations and computational setup

2.1 Flow configurations

Film-cooling hole wall models are examined using the simpler jet-in-crossflow configurations which are representative of film cooling in a turbine engine. Every configuration addressed in the following is composed of a spatially developing flat-plate boundary layer (crossflow) and a plenum issuing into the crossflow through a row of inclined holes separated by a lateral distance $P/D = 6$, where D is the hole diameter. Four hole geometries are considered (figure 1): (1) an inclined cylindrical hole; (2) the fanshaped hole of Gritsch *et al.* [27] (GFS); (3) the fanshaped laidback hole of Gritsch *et al.* [27] (GLBFS); and (4) the fanshaped laidback hole of Schroeder and Thole [66] (S&T777). The geometric parameters of the film-cooling holes are given in table 1. In each case, the hole diameter is $D = 7.75$ mm and the hole injection angle is $\alpha = 30°$. The origin O of the Cartesian coordinate system is placed at the intersection of the axis of the hole and the bottom boundary of the crossflow channel. The distance between the inlet of the domain and the center of the hole is $3.87D$. The streamwise, wall-normal and spanwise coordinates are denoted by x, y and z respectively. The azimuthal angle between the streamwise unit vector $\boldsymbol{e}_x$ and the axis of the cylinder projected orthogonally onto the bottom boundary of the crossflow channel (hereafter denoted $\boldsymbol{e}_1$) is the compound angle of the hole γ. This compound angle is independent of α and represented in figure 2. The flow is characterised by the five following nondimensional parameters:

- the freestream Reynols number $Re = U_\infty D/\nu_\infty$, where U_∞ and ν_∞ are respectively the freestream velocity and kinematic viscosity of the crossflow;
- the freestream Mach number $Ma = U_\infty/c_\infty$, where c_∞ is the freestream speed of sound of the crossflow;
- the freestream Prandtl number $Pr = \mu_\infty C_{p,\infty}/\lambda_\infty$, where μ_∞, $C_{p,\infty}$ and λ_∞ are respectively the freestream dynamic viscosity, heat capacity at constant pressure and thermal conductivity of the crossflow;
- the density ratio $DR = \rho_h/\rho_\infty$, where ρ_h and ρ_∞ are respectively the mean density of the jet at the hole entrance and the freestream density of the crossflow;
- the blowing ratio $BR = \rho_h U_h/\left(\rho_\infty U_\infty\right)$, where U_h and U_∞ are respectively the mean density-weighted velocity magnitude of the jet at the hole entrance and the freestream velocity of the crossflow.

Two types of computational domains are used to model these physical configurations: the hole-meshed computational domain and the hole-modelled computational domain. In the hole-meshed case, the crossflow channel, the plenum and the in-hole flow are simulated, as represented in figure

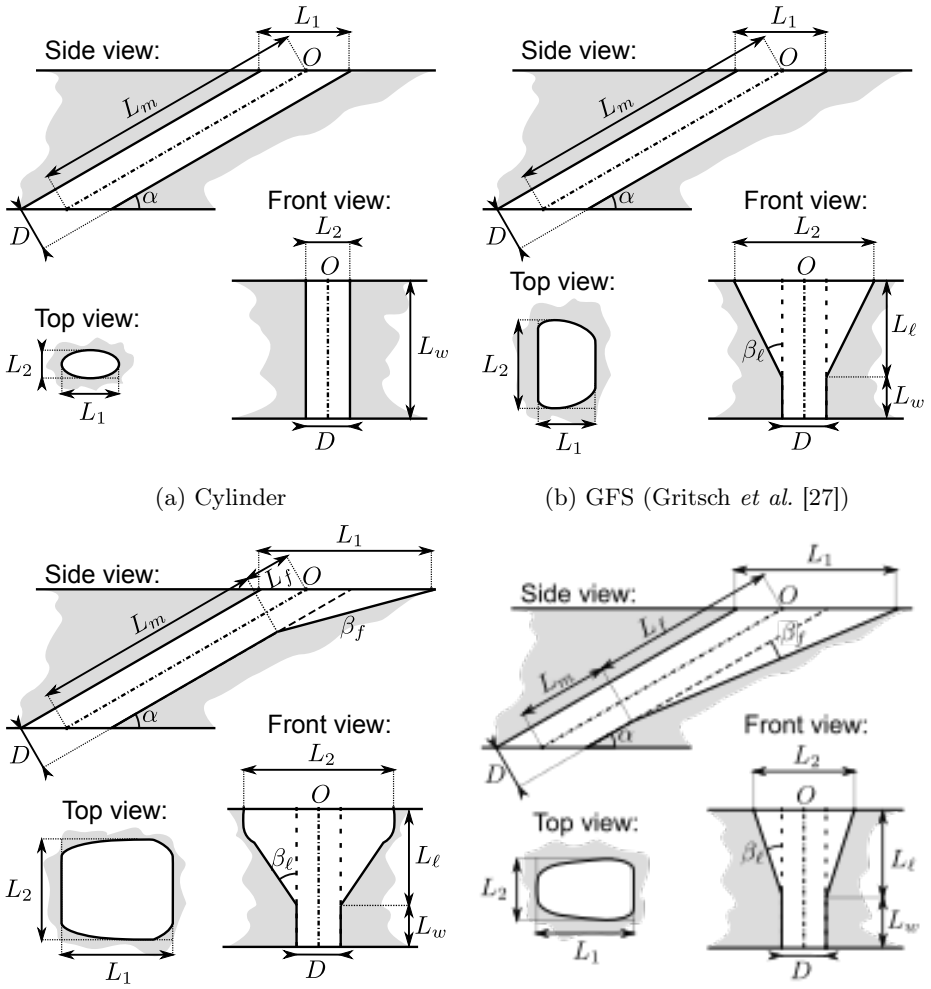

(a) Cylinder

(b) GFS (Gritsch *et al.* [27])

(c) GLBFS (Gritsch *et al.* [27])

(d) S&T777 (Schroeder and Thole [66])

Figure 1: Side, front and top view of the geometry of the film-cooling holes.

3. The size of the crossflow channel is $45D$, $13D$ and $6D$ in the streamwise, wall-normal and spanwise directions respectively while the size of the bottom plenum is $19D \times 13D \times 6D$. The plenum acts as a pressure potential that allows the blowing ratio to be imposed. The plenum size has been selected to be large enough to prevent parasite physical phenomena, such as an effect of the walls in the streamwise direction. In the hole-modelled case, only the crossflow channel is simulated whereas the jet is modelled using a wall boundary condition, as represented in figure 4. The size of the crossflow channel is the same in the hole-modelled case and the hole-meshed case. In the two cases (figures 3 and 4), only one hole is considered.

2.2 Governing equations

The numerical simulations are performed using the filtered compressible Navier–Stokes equations and the computable filtered total energy formulation,

$$\begin{aligned} \partial_t \rho + \nabla \cdot (\rho \boldsymbol{U}) &= 0, \\ \partial_t (\rho \boldsymbol{U}) + \nabla \cdot (\rho \boldsymbol{U} \otimes \boldsymbol{U}) &= -\nabla P + \nabla \cdot \boldsymbol{\Sigma}, \\ \partial_t (\rho E) + \nabla \cdot (\rho \boldsymbol{U} H) &= -\nabla \cdot \boldsymbol{Q} - \nabla \cdot (\boldsymbol{U} P) + \nabla \cdot (\boldsymbol{U} \cdot \boldsymbol{\Sigma}), \end{aligned} \tag{1}$$

where t is the time, ρ the filtered density of the fluid, $\boldsymbol{U}$ the Favre-filtered velocity, P the filtered pressure, E the Favre-filtered total energy per unit mass and $H = E + P/\rho$ the Favre-filtered total

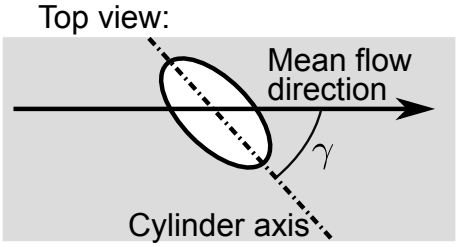

Figure 2: Compound angle γ.

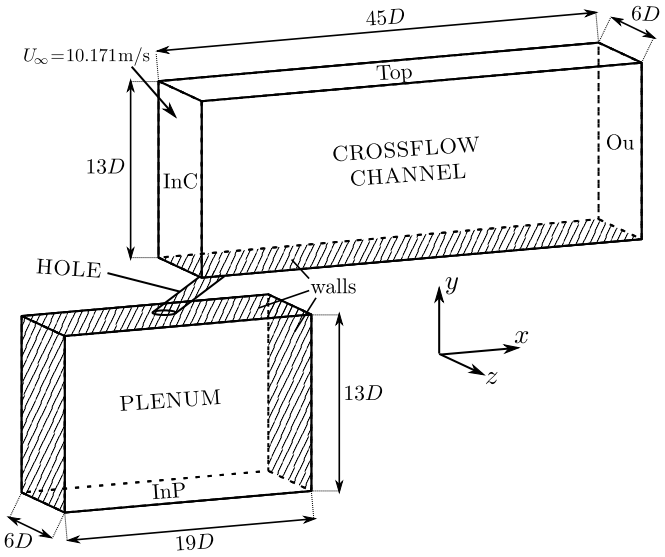

Figure 3: Hole-meshed computational domain.

enthalpy per unit mass. No body force or heat source is taken into account. The fluid is assumed to obey the ideal gas equation of state. The shear-stress tensor is computed assuming a Newtonian fluid under Stokes' hypothesis and a functional model for the subgrid-scale contribution [60],

$$\boldsymbol{\Sigma} = (\mu + \mu_{\mathrm{WALE}})\mathbf{S}^{\mathrm{dev}}, \tag{2}$$

with $\mathbf{S} = (1/2)(\nabla \boldsymbol{U} + (\nabla \boldsymbol{U})^T)$ the rate of deformation tensor and where $\mathbf{S}^{\mathrm{dev}} = \mathbf{S} - (1/3)\mathbf{I_d}\,\mathrm{tr}(\mathbf{S})$ denotes the deviatoric part of $\mathbf{S}$. The dynamic viscosity μ follows Sutherland's law [72]. The subgrid-scale viscosity is given by the WALE model [53]

$$\mu_{\mathrm{WALE}} = (C_w \Delta^2)\frac{(\mathbf{S}_d^{\mathrm{dev}} : \mathbf{S}_d^{\mathrm{dev}})^{3/2}}{(\mathbf{S} : \mathbf{S})^{5/2} + (\mathbf{S}_d^{\mathrm{dev}} : \mathbf{S}_d^{\mathrm{dev}})^{5/4}}, \tag{3}$$

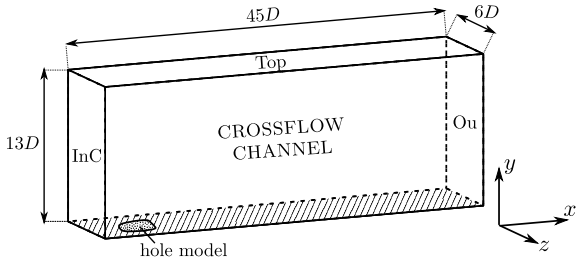

Figure 4: Hole-modelled computational domain.

with Δ the filter length scale, computed following Deardorff [17] as the cube-root of the cell volume, $\mathbf{S}_d = (1/2)(\nabla \boldsymbol{U} \nabla \boldsymbol{U} + (\nabla \boldsymbol{U} \nabla \boldsymbol{U})^T)$ the symmetric part of the squared velocity gradient tensor and $C_w = 0.47$ the model constant. The conductive heat flux is computed assuming Fourier's law and an eddy-diffusivity subgrid-scale contribution,

$$\boldsymbol{Q} = -(\lambda + \lambda_{\mathrm{WALE}}) \nabla T, \tag{4}$$

where T is the Favre-filtered temperature of the fluid. The thermal conductivity follows from a constant Prandtl number assumption. The subgrid-scale diffusivity is given by $\lambda_{\mathrm{WALE}} = C_p \mu_{\mathrm{WALE}} / Pr_{\mathrm{sgs}}$, with $Pr_{\mathrm{sgs}} = 0.6$ the subgrid-scale Prandtl number. The isobaric heat capacity C_p is computed from tabulated data [71].

2.3 Numerical setup

The governing equations are discretised and resolved using a cell-vertex finite-element method [52]. A two-step Taylor–Galerkin scheme with third-order accuracy in space and time is used for convection [15] while a centred second-order scheme is used for diffusion. At the front boundary of the crossflow channel (InC in figures 3 and 4), the velocity and temperature profiles are imposed at $\boldsymbol{U}_{\mathrm{InC}}$ and T_{InC} respectively using a non-reflecting boundary condition based on characteristic analysis [16]. The inlet velocity $\boldsymbol{U}_{\mathrm{InC}}$ follows the piecewise law of the wall

$$\boldsymbol{U}_{\mathrm{InC}} = \begin{cases} U_\tau y^+ \boldsymbol{e}_x & \text{if } \log y^+ \geq \kappa \left(y^+ - C^+\right), \\ U_\infty \boldsymbol{e}_x & \text{if } y^+ \geq \exp\left(\kappa \left(U_\infty / U_\tau - C^+\right)\right), \\ U_\tau \left(\frac{1}{\kappa} \log y^+ + C^+\right) \boldsymbol{e}_x & \text{otherwise,} \end{cases} \tag{5}$$

with $\kappa = 0.41$, $C^+ = 5.2$, $y^+ = y U_\tau / \nu$, $U_\tau = 0.513$ m/s and $U_\infty = 10.171$ m/s. The inlet temperature is $T_{\mathrm{InC}} = 295$ K. The corresponding boundary layer thickness based on 99% of U_∞ is $1.5D$. The momentum thickness Reynolds number is 730. Note that since no turbulence is injected at the inlet, this study does not consider the effect of the boundary-layer velocity fluctuations on film cooling. At the rear boundary of the crossflow channel (Ou), the pressure is imposed at $P_{\mathrm{Ou}} = 9.6871 \times 10^4$ Pa using the characteristic boundary condition of Poinsot and Lele [58]. In the hole-meshed simulation, the stagnation pressure and the stagnation temperature at the bottom boundary of the plenum (InP) are imposed at $P_{s,\mathrm{InP}}$ and $T_{s,\mathrm{InP}}$ respectively using the characteristic boundary condition of Odier *et al.* [54]. The values of $P_{s,\mathrm{InP}}$ and $T_{s,\mathrm{InP}}$ are selected in order to reach the desired mass flow rate and temperature in the hole. A symmetric boundary condition (Sym) is used on the side boundaries of the plenum. Namely, the normal velocity and the normal gradients of velocity, temperature and pressure are imposed to zero. At the top boundary of the crossflow channel (Top), a zero normal velocity and conductive heat flux are imposed while adiabatic no-slip walls are used for the top, front and rear boundaries of the plenum. Finally, the boundary condition used on the side boundaries of the crossflow channel depends on the expected numerical behaviour of the jet: For the cylindrical and S&T777 holes without compound angle, a symmetric boundary condition is used as the jet is not expected to reach the side boundaries of the domain; whereas for the GFS and GLBFS holes and the simulations with a non-zero compound angle, a periodic boundary condition is used as the jet is in these cases expected to reach the side boundaries of the domain.

The mesh parameters of the hole-meshed and hole-modelled simulations are reported in table 2. In both cases, the discretisation is fully tetrahedral. Two levels of refinement are examined in the hole-modelled simulations. The fine mesh has the same level of refinement as the hole-meshed case but around 30% less cells since the plenum is not meshed. The coarse mesh is intended to be representative of a mesh that could be used in a complex configuration and has 90% less cells than the corresponding hole-meshed simulation. Besides, the coarse mesh allows larger timesteps than the fine mesh due to the larger cell sizes, resulting in an overall cost reduction of up to 97%. A view of the fine and coarse meshes is given in figure 5. Both meshes are symmetrical with respect to the centreline plane. The distribution of the height of the first cell off the wall along the streamwise direction is compared in figure 6 for the S&T777 hole. The height of the first cell off the wall ranges from $y^+_{wall} = 4$ to 16 with the fine mesh and from $y^+_{wall} = 30$ to 55 with the coarse

Table 2: Mesh parameters of the hole-meshed and hole-modelled simulations. WCT/FTT denotes the wall-clock time required to simulate one flow-through time. $\max(y^+)$ is the maximum value of the height of the first cell off the wall, in wall units.

Geometry	Mesh	Number of nodes	Number of cells	WCT/FTT (hour)	$\max(y^+)$
Cylinder	Meshed-hole simulation	5.3×10^6	30.1×10^6	28.9	15
	Modelled-hole simulation, Fine mesh	3.5×10^6	20.0×10^6	19.6	15
	Modelled-hole simulation, Coarse mesh	0.3×10^6	1.9×10^6	0.7	44
GFS	Meshed-hole simulation	3.9×10^6	22.4×10^6	22.0	16
	Modelled-hole simulation, Fine mesh	2.8×10^6	15.7×10^6	15.3	16
	Modelled-hole simulation, Coarse mesh	0.6×10^6	3.2×10^6	1.1	43
GLBFS	Meshed-hole simulation	4.4×10^6	24.8×10^6	23.3	16
	Modelled-hole simulation, Fine mesh	3.0×10^6	17.0×10^6	18.3	16
	Modelled-hole simulation, Coarse mesh	0.3×10^6	1.6×10^6	0.7	48
S&T777	Meshed-hole simulation	3.9×10^6	22.4×10^6	21.1	16
	Modelled-hole simulation, Fine mesh	2.9×10^6	16.5×10^6	16.9	16
	Modelled-hole simulation, Coarse mesh	0.3×10^6	1.8×10^6	0.6	55

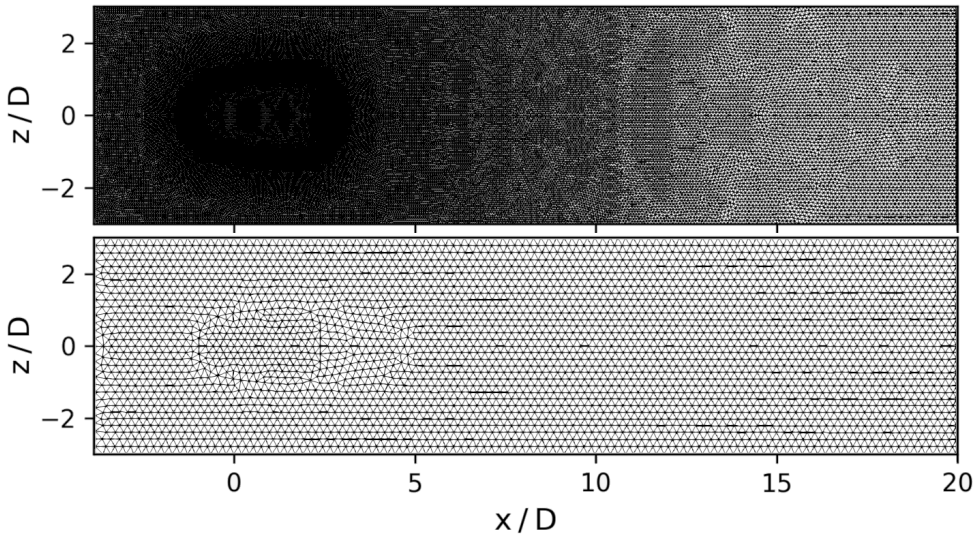

Figure 5: View of the fine mesh (top) and the coarse mesh (bottom) on the plate ($y = 0$) for the S&T777 hole in the modelled-hole case.

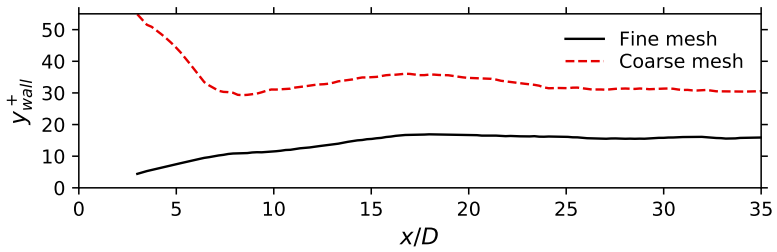

Figure 6: Centreline streamwise profile of the height of the first cell off the wall for the S&T777 hole, in wall units.

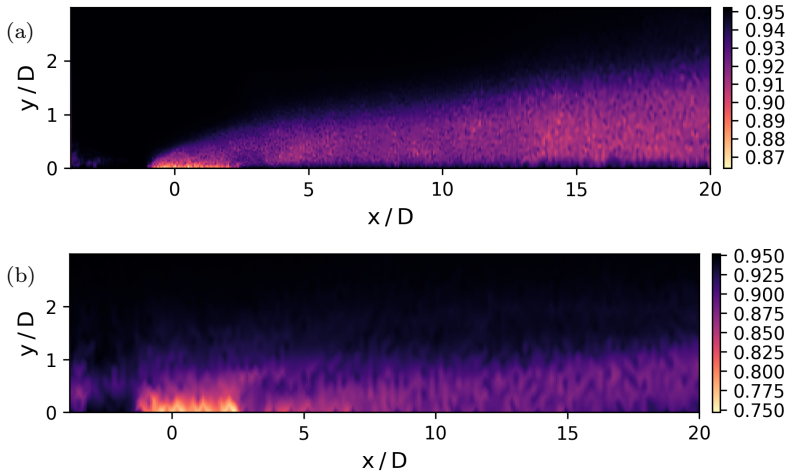

Figure 7: Celik's viscous index of resolution quality on the centreline plane ($z = 0$) for the S&T777 hole with fine mesh (a) and the coarse mesh (b).

mesh. Since the mesh is locally isotropic, the cell sizes in the streamwise and spanwise directions are similar. Celik's viscous index of resolution quality is given in figure 7. It is computed as [14]

$$\mathrm{IQ}_\nu = \frac{1}{1 + 0.05(\frac{\nu+\nu_{\mathrm{sgs}}}{\nu})^{0.53}}. \tag{6}$$

The index is above 0.88 on all computational cells with the fine mesh, which is indicative of a good large eddy simulation. With the coarse mesh, values below 0.8 are obtained for the cells next to the hole boundary condition. With the coarse mesh, the wall-normal gradient of tangential velocity is imposed assuming a law of the wall (5) at the bottom boundary of the crossflow channel, while a no-slip boundary condition is used with the fine mesh, in accordance with the hole-meshed simulations.

2.4 Film-cooling injection modelling

Although the flow inside the plenum is laminar, the flow inside the film-cooling hole transitions to turbulence as the separation region created at the entrance of the hole is destabilised [37, 48, 1]. In the hole-modelled simulations, the influence of the structure of the in-hole flow is reduced to a boundary condition corresponding to the surface of the hole exit. Several boundary-condition models are considered: a uniform injection; a non-uniform injection, taking into account the spatial variations of velocity and temperature in the in-hole flow; a turbulent uniform injection, taking into account the in-hole turbulent fluctuations; and a turbulent non-uniform injection, taking into account the spatial variations of the mean field and of turbulence intensity in the in-hole flow. Synthetic turbulence is injected isotropically using the approach of Kraichnan [38] with an integral length scale $D/(3\sqrt{2\pi})$. With the coarse mesh, turbulence cannot be represented below a wave length corresponding to twice the characteristic length of cells. The magnitude of the larger scales is thus amplified in order to preserve the flux of turbulence kinetic energy on the hole surface.

Note that the results of the hole-meshed computations are used to inform the hole-modelled simulations. If one denotes $\langle\phi_{\mathrm{mesh}}\rangle$ the statistical average of the variable ϕ in the hole-meshed computation and $\langle\langle\phi\rangle\rangle_{\mathrm{H}}$ the surface average of $\langle\phi_{\mathrm{mesh}}\rangle$ over the surface $\mathcal{S}_{\mathrm{H}}$ corresponding to the hole exit, such that

$$\langle\langle\phi_{\mathrm{mesh}}\rangle\rangle_{\mathrm{H}} = \frac{\int_{\mathcal{S}_{\mathrm{H}}} \langle\phi_{\mathrm{mesh}}\rangle \, dx \, dy}{\int_{\mathcal{S}_{\mathrm{H}}} dx \, dy}, \tag{7}$$

the velocity and temperature profiles in the case of a uniform injection are imposed at $\boldsymbol{U}_{\mathrm{HU}} = \langle\langle\rho_{\mathrm{mesh}}\boldsymbol{U}_{\mathrm{mesh}}\rangle\rangle_{\mathrm{H}} / \langle\langle\rho_{\mathrm{mesh}}\rangle\rangle_{\mathrm{H}}$ and $T_{\mathrm{HU}} = 1/\langle\langle 1/T_{\mathrm{mesh}}\rangle\rangle_{\mathrm{H}}$ respectively, in order to conserve the

same mass flow rate in the hole-meshed and hole-modelled simulations. In the case of a non-uniform injection, the velocity and temperature profiles are imposed using respectively the local mean density-weighted velocity and the local mean temperature of the hole-meshed computation. In the case of a turbulent uniform injection, the velocity and temperature profiles are imposed at $\boldsymbol{U}_{\mathrm{HU}}$ and T_{HU} respectively while the turbulence kinetic energy per unit mass $k = (1/2)\sum_i u_i'^2$, where $u_i = U_i - \langle U_i \rangle$ is the fluctuation of velocity, is set to $k_{\mathrm{HU}} = \langle\langle \rho_{\mathrm{mesh}} k_{\mathrm{mesh}} \rangle\rangle_{\mathrm{H}} \,/\, \langle\langle \rho_{\mathrm{mesh}} \rangle\rangle_{\mathrm{H}}$. In the case of a turbulent non-uniform injection, the velocity, temperature and turbulence kinetic energy profiles are imposed using respectively the local mean density-weighted velocity, the local mean temperature and the local density-weighted turbulence kinetic energy per unit mass of the hole-meshed computation.

2.5 Validation

The numerical simulations are performed using the hybrid flow solver AVBP [65] which has been extensively validated in various physical configurations [see e.g. 24, 25, 18]. In order to validate the present numerical setup, this section focuses on the comparison of the hole-meshed numerical simulations with the experimental data of Schroeder and Thole [66]. Indeed, the inlet Reynolds number, inlet Mach number, inlet boundary-layer thickness and the temperature levels of the numerical simulations are consistent with these experiments contrarily to the other geometries. The geometry is also similar to that of figures 3 and 4. Figure 8 compares the numerical and experimental mean adiabatic effectiveness for a blowing ratio DR=1.5. The adiabatic effectiveness corresponds here to the nondimensionalised temperature at the wall,

$$\theta = \frac{T_\infty - T}{T_\infty - T_h}, \tag{8}$$

where T_∞ is the freestream temperature of the crossflow and T_h the mean temperature of the jet. Overall, there is a good agreement between the numerical and the experimental thermal footprints. The main difference lies in the level of adiabatic effectiveness outside the influence of the jet, which is nonzero in the experimental data but vanishes in the numerical simulation. The discrepancy can be attributed to conductive processes within the plate material (polystyrene) that the adiabatic boundary condition used in the simulation cannot reproduce [68]. In addition, there is in the experiment a slight lateral deviation of the jet with respect to the centreline plane (figure 9, left). These two effects influence the profile of the centreline adiabatic effectiveness and may explain the slightly larger value obtained in the numerical simulation throughout the plate compared to the experimental data, despite an otherwise similar behaviour (figure 9, right). Figure 10 compares the centreline adiabatic effectiveness obtained for the GFS and GLBFS holes to the experimental campaign of Gritsch *et al.* [27]. As for the S&T777 hole, there is in both cases a reasonable level of agreement between the numerical and experimental centreline adiabatic effectivenesses but the predicted values are larger in the numerical simulations than in the experiments. Note that the experiments of Gritsch *et al.* [27] and Schroeder and Thole [66] report a free-stream turbulence level of 2% and 0.5% respectively whereas there is no turbulence injection at the inlet of the domain in the simulations, as described in section 2.3. The present validation results confirm that such low freestream turbulence levels can be approximated as if there are no disturbances in the freestream. Note however that such assumptions does not hold generally [70].

3 Results and discussion

This section compares the accuracy of the film-cooling hole wall models presented in section 2.4 in the various configurations. All film-cooling configurations investigated in this paper lead to a fully turbulent film downstream the hole. The density ratios, blowing ratios and compound angles of the selected configurations are reported in table 3. For models with a non-uniform fluid injection, the distributions of velocity magnitude at the hole exit is presented in figure 11 and the distributions of turbulence kinetic energy in figure 12. In each case, the performance of a boundary-condition model is assessed from the comparison of the results of a simulation using this

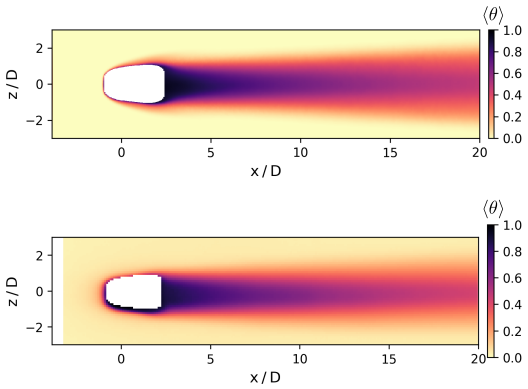

Figure 8: Mean adiabatic effectiveness on the plate ($y = 0$) for the S&T777 hole at BR=1.5 without compound angle in the hole-meshed numerical simulation (top) and the experimental campaign of Schroeder and Thole [66] (bottom).

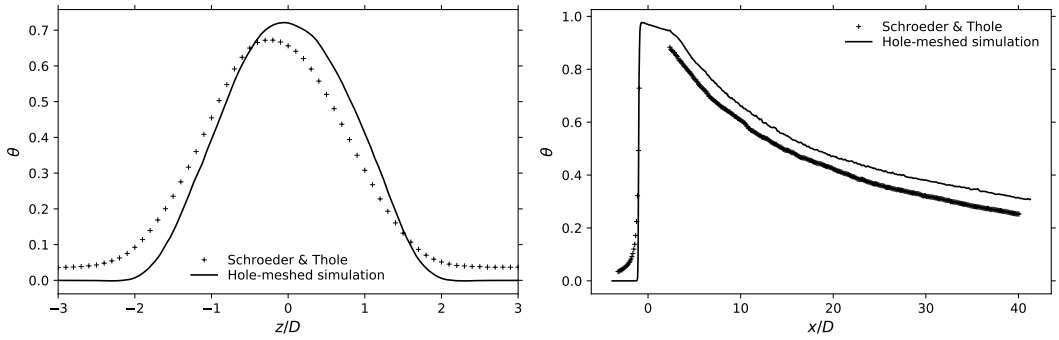

Figure 9: Mean spanwise profile of adiabatic effectiveness at x/D=8 (left) and centreline streamwise profile of adiabatic effectiveness (right) on the plate ($y = 0$) for the S&T777 hole at BR=1.5 without compound angle in the hole-meshed numerical simulation and the experimental campaign of Schroeder and Thole [66].

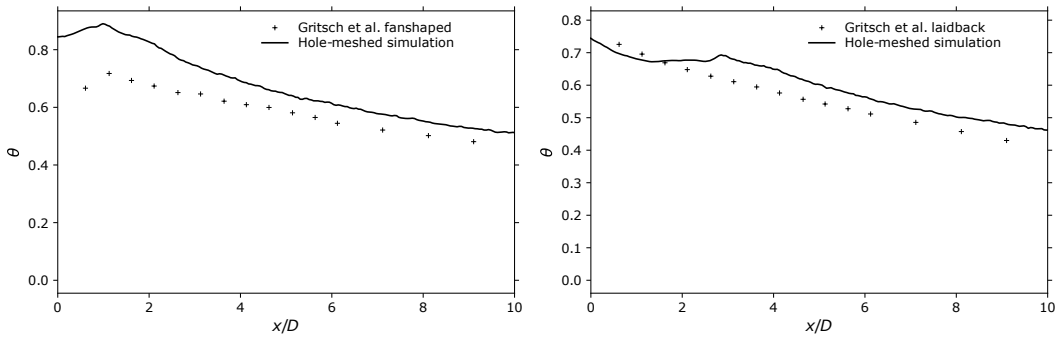

Figure 10: Mean centreline streamwise profile of adiabatic effectiveness on the plate ($y = 0$) for the GFS hole (left) and the GLBFS hole at BR=1.5 without compound angle in the hole-meshed numerical simulation and the experimental campaign of Gritsch *et al.* [27].

Table 3: Plenum stagnation pressure, plenum stagnation temperature, blowing ratio and density ratio for the different hole-meshed simulations.

Simulation	$P_{s,\mathrm{InP}}$, Pa	$T_{s,\mathrm{InP}}$, K	DR	BR
Cylinder BR=1.5 γ=0°	9.7105×10^4	1.980×10^2	1.48	1.53
Cylinder BR=0.5 γ=0°	9.6917×10^4	1.980×10^2	1.49	0.48
Cylinder BR=0.5 γ=60°	9.6924×10^4	1.980×10^2	1.49	0.50
GFS BR=1.5 γ=0°	9.7066×10^4	1.980×10^2	1.50	1.39
GLBFS BR=1.5 γ=0°	9.7089×10^4	1.980×10^2	1.49	1.60
S&T777 BR=1.5 γ=0°	9.7031×10^4	1.980×10^2	1.49	1.50
S&T777 BR=1.5 γ=60°	9.7063×10^4	1.980×10^2	1.49	1.60
S&T777 BR=3.0 γ=0°	9.7469×10^4	1.980×10^2	1.48	3.05
S&T777 BR=2.5 γ=0°	9.7292×10^4	1.980×10^2	1.48	2.55
S&T777 BR=2.0 γ=0°	9.7150×10^4	1.980×10^2	1.49	2.03
S&T777 BR=1.0 γ=0°	9.6946×10^4	1.980×10^2	1.49	0.97
S&T777 BR=0.5 γ=0°	9.6903×10^4	1.980×10^2	1.49	0.48

model with the corresponding hole-meshed simulation. To this end, the concordance correlation coefficient of Lin [45] is used to give a measure of the agreement between the mean fields of two simulations. The concordance correlation coefficient between the statistical average of variable ϕ in the hole-meshed computation, denoted $\langle\phi_{\mathrm{mesh}}\rangle$, and the corresponding statistical average in the hole-modelled computation, denoted $\langle\phi_{\mathrm{mod}}\rangle$, is given by

$$C_\phi^{\mathcal{V}} = \frac{\langle\langle\phi_{\mathrm{mesh}}\rangle\,\langle\phi_{\mathrm{mod}}\rangle\rangle_{\mathcal{V}} - \langle\langle\phi_{\mathrm{mesh}}\rangle\rangle_{\mathcal{V}}\,\langle\langle\phi_{\mathrm{mod}}\rangle\rangle_{\mathcal{V}}}{\left\langle\langle\phi_{\mathrm{mesh}}\rangle^2\right\rangle_{\mathcal{V}} - \langle\langle\phi_{\mathrm{mesh}}\rangle\rangle_{\mathcal{V}}^2 + \left\langle\langle\phi_{\mathrm{mod}}\rangle^2\right\rangle_{\mathcal{V}} - \langle\langle\phi_{\mathrm{mod}}\rangle\rangle_{\mathcal{V}}^2 + (\langle\langle\phi_{\mathrm{mesh}}\rangle\rangle_{\mathcal{V}} - \langle\langle\phi_{\mathrm{mod}}\rangle\rangle_{\mathcal{V}})^2}, \quad (9)$$

where $\langle\,\cdot\,\rangle_{\mathcal{V}}$ is a volume average over the computational domain of the hole-modelled simulation. A value of one indicates that the two fields are identical. Finally, note that the ensemble average $\langle\,\cdot\,\rangle$ is taken to be a time average in practice. A minimal averaging duration of 3 flow-through time is used to converge the statistics for all simulations.

We first investigate the performance of the models with the fine mesh in section 3.1 and with the coarse mesh in section 3.2.

3.1 Effect of the film-cooling hole wall model

3.1.1 Inclined cylindrical hole

This section compares the performance of hole-modelled simulations with a uniform, non-uniform, turbulent uniform and turbulent non-uniform injection for an inclined cylindrical hole using the fine mesh, that is with the same level of mesh refinement as the reference hole-meshed simulations. The results are summarised in table 4 using several global measures of the performance of the models. The concordance correlation coefficients suggest that the quality of the predictions with the baseline uniform model is low at the larger blowing ratio BR=1.5, especially in regard to the fields of temperature, turbulence kinetic energy and standard deviation of temperature. For instance, the corresponding concordance correlation coefficient of the standard deviation of temperature on the plane $y = 0$ ($C^{\mathcal{P}}_{T'^2}$) is 0.024, which is indicative of a very poor agreement. The table also suggests that the disagreement is resolved using a turbulent injection, as the value of $C^{\mathcal{P}}_{T'^2}$ is for instance increased to 0.952, which indicates a good level of agreement. These points are investigated in more detail in the following.

The capability of the boundary-condition model to generate a turbulent jet depends on the hole geometry and nondimensional parameters, notably the density ratio and the blowing ratio. In the case of a cylindrical hole at BR=1.5 without compound angle, a hole model without turbulence injection leads to a laminar jet over a large portion of the domain as the destabilisation of the jet by the crossflow is not sufficient to trigger transition (figure 13). The addition of synthetic

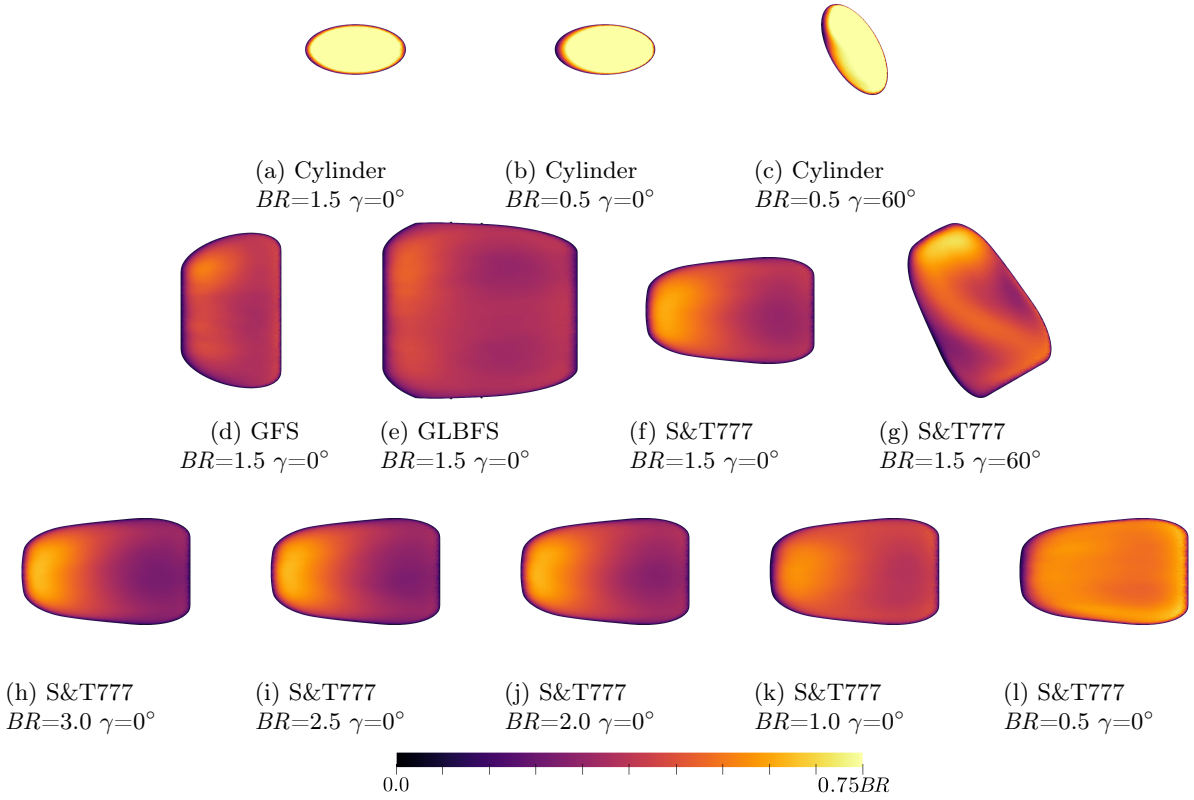

Figure 11: Mean nondimensionalised velocity magnitude at the hole exit in the hole-meshed simulations.

Table 4: (Colour online) Agreement between the hole-meshed simulations and the fine-mesh hole-modelled simulations with a uniform injection (UI), a non-uniform injection (NI), a turbulent uniform injection (TUI) and a turbulent non-uniform injection (TNI) for an inclined cylindrical hole. The volume average $\langle\cdot\rangle_{\mathcal{V}}$ is performed on the whole domain up to $x = 0.35D$. The surface average $\langle\cdot\rangle_{\mathcal{P}}$ is performed on the plane $y = 0$ between $x = 4D$ and $x = 20D$. The length $d_{\overline{\mathcal{S}}}$ is the root-mean-square distance between the mean streamline $\overline{\mathcal{S}}$ (defined below, see equation (11)) of the hole-modelled simulation and of the hole-meshed simulation. 'A' indicates the attachment of the jet to the wall and 'D' the detachment of the jet from the wall. An asterisk is appended to the letter if the behaviour is different in the hole-meshed simulation. The columns are tinted in blue if the ideal value of the measure is zero. Conversely, the columns are tinted in red if the ideal value is zero.

Simulation		$\frac{\langle\langle T-T_{\mathrm{ref}}\rangle\rangle_{\mathcal{P}}}{\sqrt{\langle\langle T_{\mathrm{ref}}\rangle^2\rangle_{\mathcal{P}}}}$	$C_T^{\mathcal{P}}$	$C_{T'^2}^{\mathcal{P}}$	$C_T^{\mathcal{V}}$	$C_{\lvert\boldsymbol{U}\rvert}^{\mathcal{V}}$	$C_k^{\mathcal{V}}$	$d_{\overline{\mathcal{S}}}/D$	
Cylinder BR=1.5 γ=0°	UI	0.12	0.652	0.024	0.722	0.940	0.010	0.37	D
Cylinder BR=1.5 γ=0°	NI	0.76	0.506	0.010	0.683	0.934	0.044	1.30	D
Cylinder BR=1.5 γ=0°	TUI	0.10	0.945	0.952	0.994	0.993	0.920	0.81	D
Cylinder BR=1.5 γ=0°	TNI	0.05	0.990	0.981	0.998	0.995	0.985	0.03	D
Cylinder BR=0.5 γ=0°	UI	0.34	0.647	0.526	0.912	0.989	0.852	0.08	D*
Cylinder BR=0.5 γ=0°	NI	0.01	0.952	0.709	0.958	0.996	0.928	0.43	D*
Cylinder BR=0.5 γ=0°	TUI	0.15	0.935	0.918	0.979	0.996	0.967	0.22	A
Cylinder BR=0.5 γ=0°	TNI	0.03	0.991	0.956	0.992	0.997	0.981	0.18	A
Cylinder BR=0.5 γ=60°	UI	0.09	0.905	0.812	0.920	0.989	0.912	0.27	A
Cylinder BR=0.5 γ=60°	NI	0.05	0.973	0.914	0.983	0.994	0.965	0.13	A
Cylinder BR=0.5 γ=60°	TUI	0.09	0.973	0.928	0.948	0.991	0.952	0.29	A
Cylinder BR=0.5 γ=60°	TNI	0.00	0.995	0.956	0.995	0.995	0.985	0.14	A
		0 0.5 1	0 0.5 1	0 0.5 1	0 0.5 1	0 0.5 1	0 0.5 1	0 0.5 1	

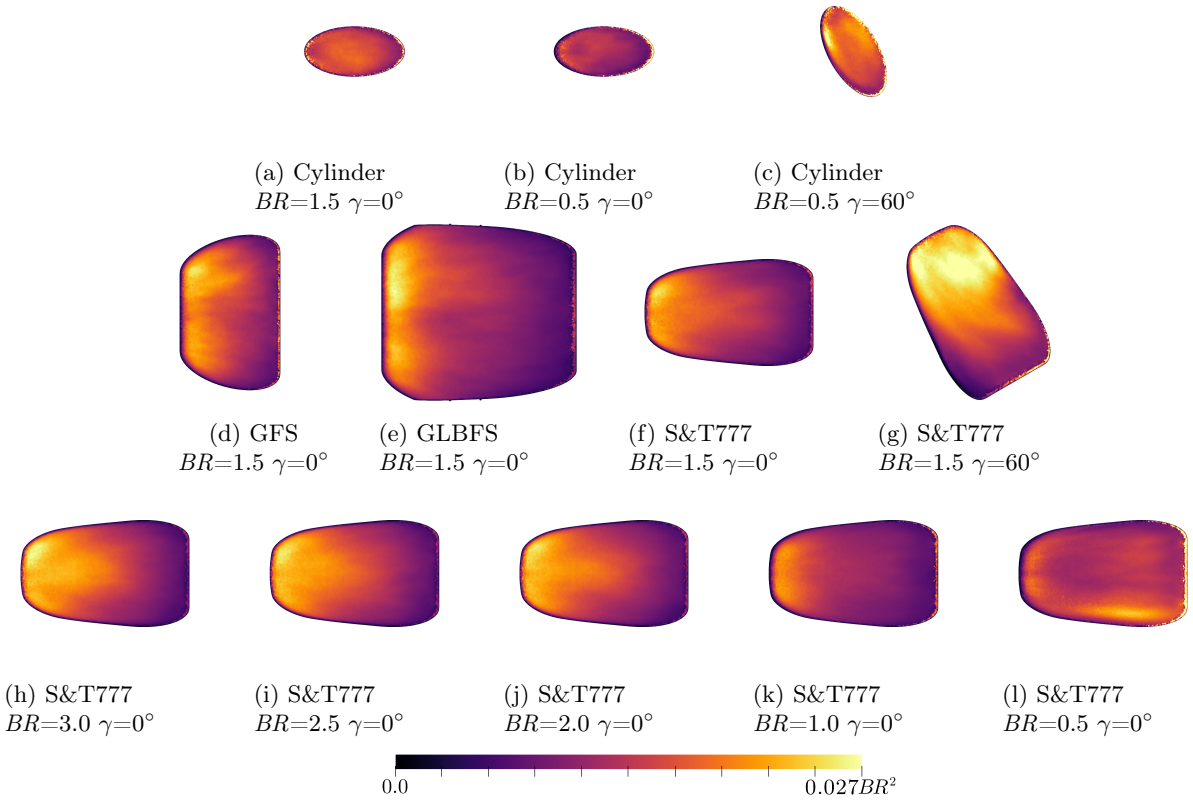

Figure 12: Mean turbulence kinetic energy at the hole exit in the hole-meshed simulations.

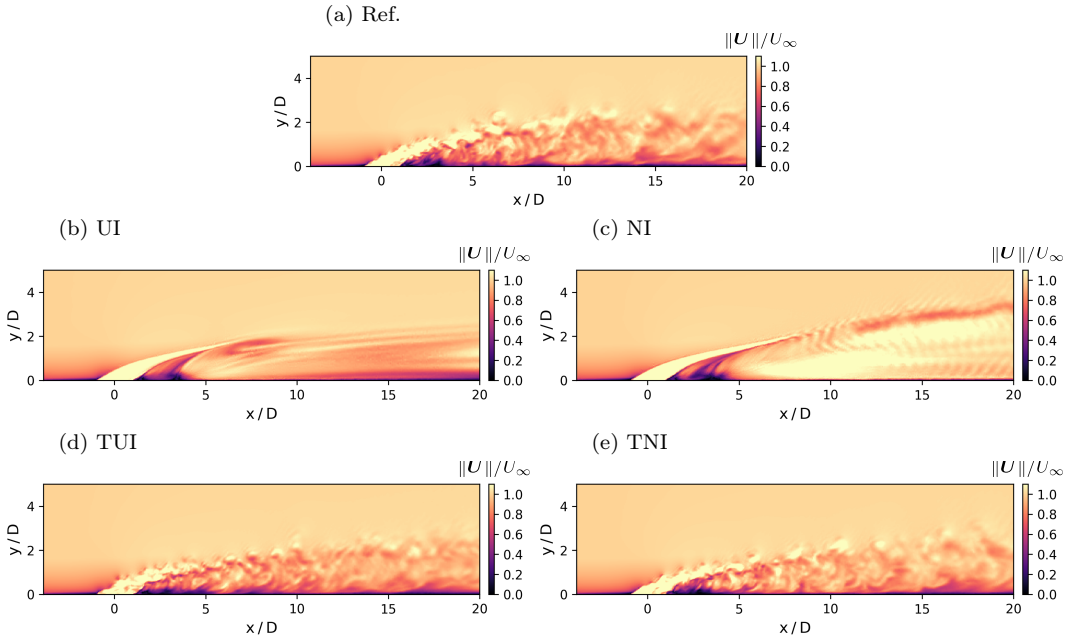

Figure 13: Instantaneous nondimensionalised velocity magnitude on the centreline plane ($z = 0$) for an inclined cylindrical hole at BR=1.5 without compound angle in the hole-meshed simulation (a) and the fine-mesh hole-modelled simulations with a uniform injection (b), a non-uniform injection (c), a turbulent uniform injection (d) and a turbulent non-uniform injection (e).

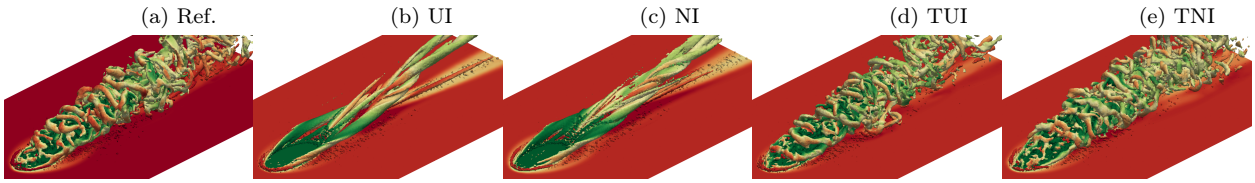

Figure 14: (Colour online) Instantaneous contour of Q criterion ($Q = 5.0 \times 10^6$ s^{-2}) around the hole exit for an inclined cylindrical hole at BR=1.5 without compound angle in the hole-meshed simulation (a) and the fine-mesh hole-modelled simulations with a uniform injection (b), a non-uniform injection (c), a turbulent uniform injection (d) and a turbulent non-uniform injection (e). The surfaces are coloured by temperature, with green-coloured regions denoting colder fluid.

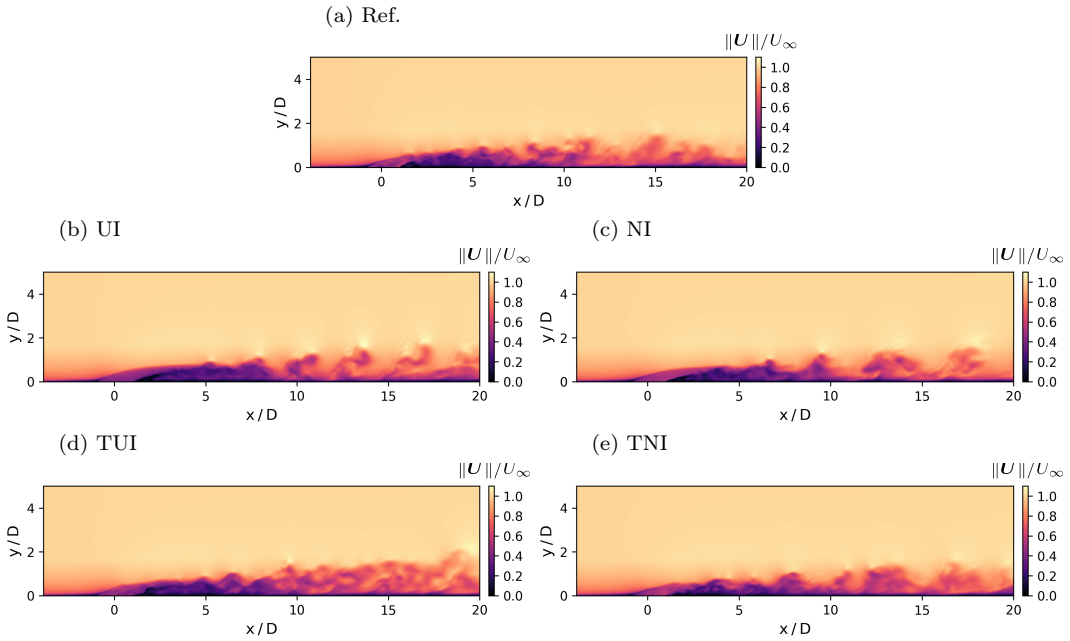

Figure 15: Instantaneous nondimensionalised velocity magnitude on the centreline plane ($z = 0$) for an inclined cylindrical hole at BR=0.5 without compound angle in the hole-meshed simulation (a) and the fine-mesh hole-modelled simulations with a uniform injection (b), a non-uniform injection (c), a turbulent uniform injection (d) and a turbulent non-uniform injection (e).

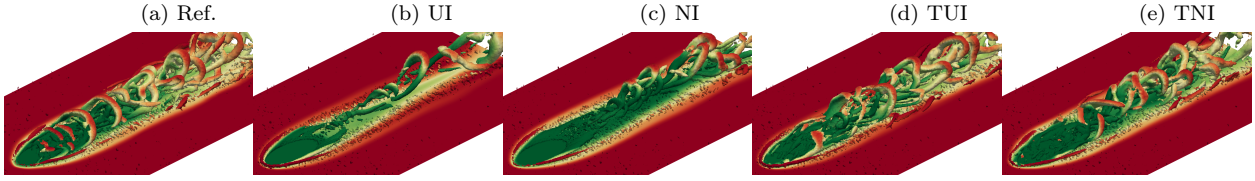

Figure 16: (Colour online) Instantaneous contour of Q criterion ($Q = 1.7 \times 10^6$ s^{-2}) around the hole exit for an inclined cylindrical hole at BR=0.5 without compound angle in the hole-meshed simulation (a) and the fine-mesh hole-modelled simulations with a uniform injection (b), a non-uniform injection (c), a turbulent uniform injection (d) and a turbulent non-uniform injection (e). The surfaces are coloured by temperature, with green-coloured regions denoting colder fluid.

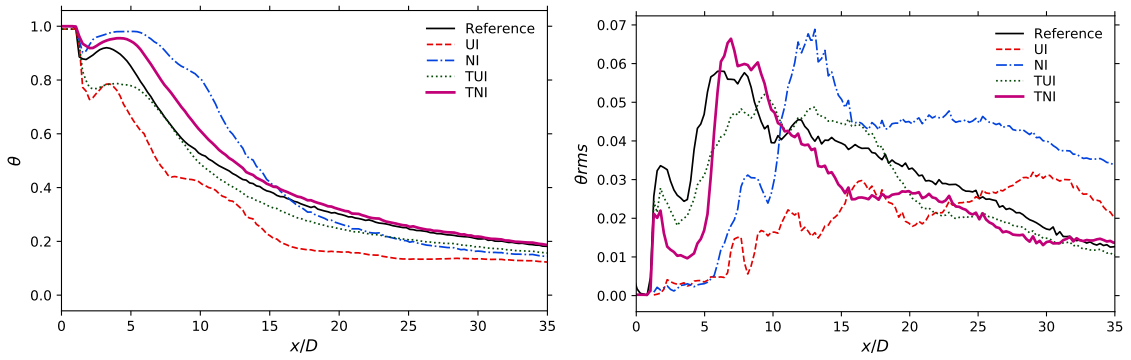

(a) $z = 0$ (centreline plane)

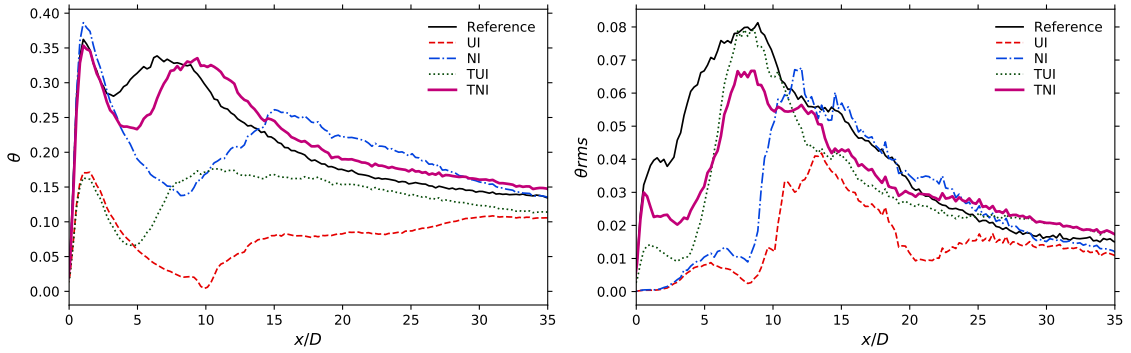

(b) $z = D$

Figure 17: Mean adiabatic effectiveness (left) and standard deviation of adiabatic effectiveness (right) for an inclined cylindrical hole at BR=0.5 without compound angle in the hole-meshed simulation, the fine-mesh hole-modelled simulations with a uniform injection, a non-uniform injection, a turbulent uniform injection and a turbulent non-uniform injection.

turbulence to the boundary condition greatly improves the prediction of the jet behaviour which becomes fully turbulent. In particular, characteristic hairpin vortex structures are formed outside of the cooling hole, as identified in figure 14(d,e) by contours of Q criterion, defined as

$$Q = \frac{1}{2}\left(\mathbf{\Omega} : \mathbf{\Omega} - \mathbf{S}^{\mathrm{dev}} : \mathbf{S}^{\mathrm{dev}}\right), \tag{10}$$

with $\mathbf{\Omega} = (1/2)(\nabla \boldsymbol{U} - (\nabla \boldsymbol{U})^T)$ the rate of rotation tensor. At a lower blowing ratio BR=0.5, the jet remains attached to the plate surface and forms a film of cold fluid near the wall. The film is destabilised quite rapidly in all simulations, including those with a hole model without turbulence injection (figure 15). However, the addition of synthetic turbulence injection accelerates the transition process and improves the transition onset, as illustrated by figure 16. Accordingly, the standard deviation of adiabatic effectiveness starts increasing at the downstream boundary of the hole in simulations with synthetic turbulence injection while it only starts increasing further downstream without turbulence injection (figure 17(a), right). The profile of adiabatic effectiveness along the centreline, provided in figure 17(a), is in all hole-modelled simulations consistent to some degree with the reference profile obtained in the hole-meshed simulation. Farther from the centreline however, only the simulation with a turbulent non-uniform injection is able to reproduce the behaviour of the reference simulation (figure 17(b), left), as (a) the simulations without turbulence injection capture less accurately the mixing and lateral spreading of the jet, resulting in a delay in the location of the secondary peak of adiabatic effectiveness ($x/D = 7$); and (b) the spatial variations of mean velocity and temperature at the exit of the hole have a large impact on the adiabatic effectiveness in the near-hole region which persists throughout the channel. Taking into account the spatial inhomogeneity of the injection has on the other hand a relatively small effect on the standard deviation of adiabatic effectiveness (figure 17(b), right).

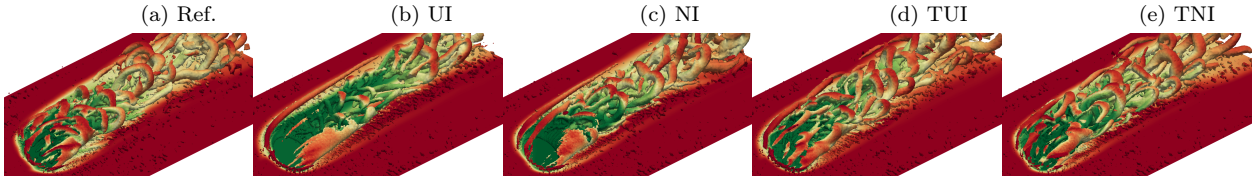

Figure 18: (Colour online) Instantaneous contour of Q criterion ($Q = 1.7 \times 10^6$ s^{-2}) around the hole exit for an inclined cylindrical hole at BR=0.5 with a compound angle γ=60° in the hole-meshed simulation (a) and the fine-mesh hole-modelled simulations with a uniform injection (b), a non-uniform injection (c), a turbulent uniform injection (d) and a turbulent non-uniform injection (e). The surfaces are coloured by temperature, with green-coloured regions denoting colder fluid.

The addition of a compound angle to the configuration further increases the destabilisation of the jet by the crossflow and further depreciates the usefulness of turbulence injection. Indeed, a compound angle injection tends to increase the mixing of the jet within the crossflow and accelerates transition. In that case, a fully turbulent film can be obtained without turbulence injection (figure 18). The thermal footprint obtained with all models is hence very similar, as shown in figure 19. Figure 20 gives the mean adiabatic effectiveness along the mean streamline $\overline{\mathcal{S}}$ projected orthogonally onto the bottom boundary of the crossflow channel. The mean streamline $\overline{\mathcal{S}}$ provides an estimation of the trajectory of the jet within the crossflow, provided that this trajectory exists. It is defined as the average of a set of streamline weighted by the velocity magnitude at the hole surface. Each individual streamline is computed from the time-averaged velocity fields using the variable-order Runge–Kutta method of Cash and Karp [13]. Then, if one denotes $\mathcal{S}_{\boldsymbol{a}}$ the streamline associated with the position vector $\boldsymbol{r}_{\boldsymbol{a}}(\eta)$ such that $\boldsymbol{r}_{\boldsymbol{a}}(0) = \boldsymbol{a}$, where η is the virtual time along the streamline path, the mean streamline $\overline{\mathcal{S}}$ associated with the position vector $\overline{\boldsymbol{r}}$ is defined as

$$\overline{\boldsymbol{r}}(\eta) = \frac{\sum_{j=1}^{N} \boldsymbol{r}_{\boldsymbol{a}_j}(\eta) \left\langle \|\boldsymbol{U}\| \right\rangle (\boldsymbol{a}_j)}{\sum_{j=1}^{N} \left\langle \|\boldsymbol{U}\| \right\rangle (\boldsymbol{a}_j)}, \tag{11}$$

with $\boldsymbol{a}_j = (-D + (L_1/N)j)\,\boldsymbol{e}_1$ and $N = 100$ the number of streamlines used for the average. The results of the hole-modelled simulation with a non-uniform or turbulent non-uniform injection are almost indistinguishable from the results of the reference hole-meshed simulation for both the mean adiabatic effectiveness (figure 19(a)) and the standard deviation of adiabatic effectiveness (figure 19(b)). All in all, the addition of synthetic turbulence injection is not necessary to trigger transition in that case, whereas synthetic turbulence injection is necessary in the case DR=1.5 without compound angle.

3.1.2 Shaped holes

Shaped holes may give rise to a more complex physics than inclined cylindrical holes. With regard to the hole-exit modelling in particular, the forward and lateral expansion of the hole creates local areas of adverse pressure gradients that may cause intermittent entrance of hot fluid within the hole. The film-cooling hole models must thus not only act as an inlet but also intermittently or locally as an outlet. The presence of instantaneous regions of backflow greatly enhances the mixing of hot and cold fluid within the hole which then leads to large temperature fluctuations on the hole surface, whereas these were negligible for a cylindrical hole. The results of hole-modelled simulations for shaped holes are summarised in table 5. The shaped holes investigated are the fanshaped and fanshaped laidback holes of Gritsch *et al.* [27] and the fanshaped laidback hole of Schroeder and Thole [66], whose geometry is given in figure 1. In both cases, the table shows that a hole model taking into account the spatial variations of the mean fields and the turbulence intensity at the hole exit provides more accurate results, similarly to what was observed above in the case of an inclined cylindrical hole. For example, an accurate prediction of the centreline adiabatic effectiveness is only obtained with a turbulent non-uniform injection for the S&T777 hole at BR=2.5 (figure 21), as the simulations with a uniform injection, a non-uniform injection or a turbulent uniform injection incorrectly predict the detachment of the jet from the wall. As for the

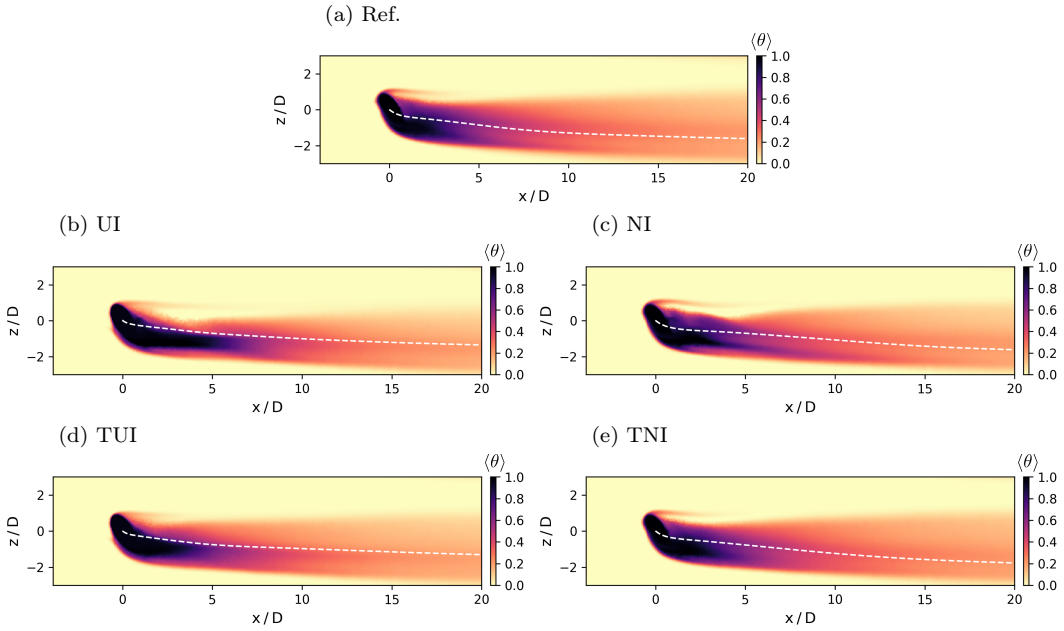

Figure 19: Mean adiabatic effectiveness on the plate ($y = 0$) for an inclined cylindrical hole at BR=0.5 with a compound angle γ=60° in the hole-meshed simulation (a) and the fine-mesh hole-modelled simulations with a uniform injection (b), a non-uniform injection (c), a turbulent uniform injection (d) and a turbulent non-uniform injection (e). The white dashed lined represents the mean streamline $\overline{\mathcal{S}}$ projected orthogonally onto the bottom boundary of the crossflow channel (refer to section 3.1.1 for details).

cylindrical hole, a non-zero compound angle does not seem more difficult to handle for the model than a zero compound angle. Figure 22 shows for instance that the turbulent non-uniform injection improves drastically the prediction of the thermal footprint for the simulation of the S&T777 hole with a compound angle of 60°.

However, the hole-modelled simulations are in general less accurate than for the cylindrical configuration and several discrepancies may be observed. Most of these issues may ultimately generally be attributed to a lack of mixing and turbulence intensity in the hole-modelled simulations. For instance, although a turbulent non-uniform injection greatly improves the prediction of the mean turbulence kinetic energy compared to the baseline uniform model with the S&T777 hole at BR=1.5, the predicted values remain lower than in the hole-meshed simulation throughout the channel (figure 23).

Similarly, the standard deviation of adiabatic effectiveness on the plate is clearly underestimated in the hole-modelled simulations (figure 24). The lack of temperature fluctuation on the hole surface with the hole models could explain some of the discrepancies in the region directly downstream the hole exit. We investigated naive corrections to the models by adding temperature fluctuations to the turbulence injection, either uncorrelated to the velocity components or negatively correlated with the wall-normal velocity component. However, these corrections had a negligible effect on the standard deviation of adiabatic effectiveness downstream the hole. Besides, note that the intensity of turbulence downstream the hole is related to the turbulent structures formed outside of the cooling hole, which are not reproduced accurately by the hole-modelled simulations. In the hole-modelled simulations, the vortices are thin, elongated in the streamwise direction and do not exhibit the characteristic horseshoe structures observed in the hole-meshed numerical simulations. This is shown in figure 25 for the GFS hole, figure 26 for the GLBFS hole and figure 27 for the S&T777 hole.

The lack of turbulence in the hole-modelled simulations results in a lack of mixing which directly affects the predicted thermal footprint. With the GLBFS hole at BR=1.5, the wall adiabatic effectiveness is significantly more accurate in the turbulent non-uniform case than using a uniform

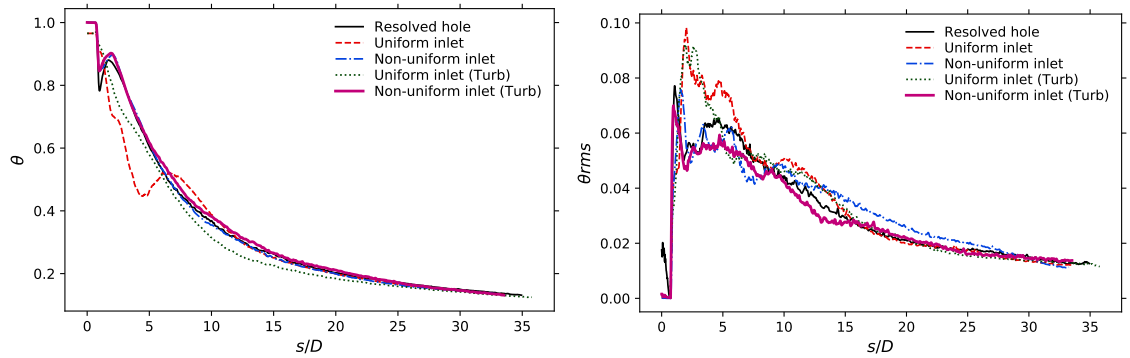

Figure 20: Mean adiabatic effectiveness (left) and standard deviation of adiabatic effectiveness (right) along the mean streamline $\overline{\mathcal{S}}$ (refer to section 3.1.1 for details) for an inclined cylindrical hole at BR=0.5 with a compound angle γ=60° in the hole-meshed simulation, the fine-mesh hole-modelled simulations with a uniform injection, a non-uniform injection, a turbulent uniform injection and a turbulent non-uniform injection.

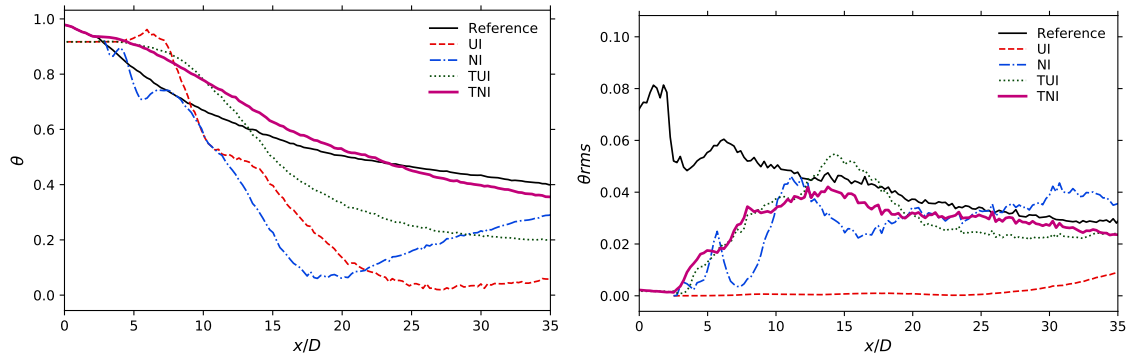

Figure 21: Centreline adiabatic effectiveness for the S&T777 hole at BR=2.5 without compound angle in the hole-meshed simulation, the fine-mesh hole-modelled simulations with a uniform injection, a non-uniform injection, a turbulent uniform injection and a turbulent non-uniform injection.

injection (figure 28), but the result also exhibits a more pronounced bimodal spanwise profile than the hole-meshed simulation throughout the plate due to the lack of temperature mixing. In the more common case of a unimodal thermal footprint, the lower temperature mixing tends to increase the adiabatic effectiveness since the vertical and lateral spreading of the jet is reduced. The effects are the most salient with the S&T777 hole at the lower blowing ratio BR=1.5. Indeed, figure 29(left) clearly shows that in that case the centreline adiabatic effectiveness only starts decreasing after $x = 6D$ in the hole-modelled simulations with synthetic turbulent injection, coincidentally with a large increase of standard deviation of adiabatic effectiveness (figure 29(right)), whereas the decrease occurs directly downstream the hole in the reference hole-meshed simulation. An accurate adiabatic effectiveness level is nevertheless obtained from $x/D = 20$ onwards. As shown by figure 21 at a higher blowing ratio BR=2.5, an overestimation of the adiabatic effectiveness in the region directly downstream the hole exit is observed to a lesser extent in other configurations.

Finally, note that in several configurations, taking into account the spatial variations of velocity and temperature at the hole exit without synthetic turbulence injection is detrimental to the results. For instance, the centreline adiabatic effectiveness is less accurate with a non-turbulent non-uniform injection than with the baseline uniform injection with the S&T777 hole at BR=0.5 (figure 29). This type of modelling may thus not be recommended in the general case. On the other hand, the addition of synthetic turbulence to the hole model is found to be consistently beneficial. The turbulent non-uniform film-cooling wall model provides the most accurate results

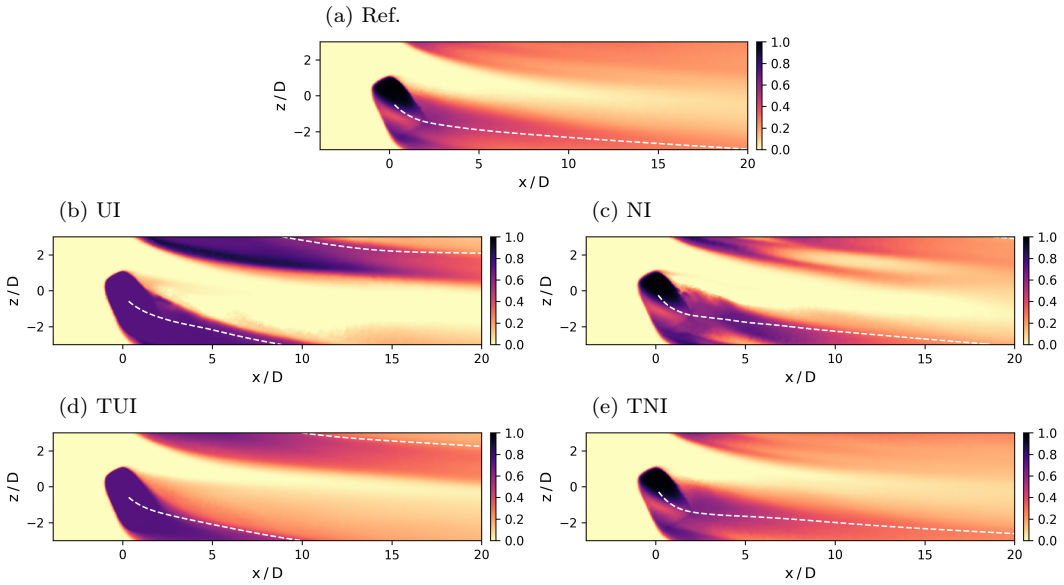

Figure 22: Mean adiabatic effectiveness on the plate ($y = 0$) for the S&T777 hole at BR=1.5 with a compound angle γ=60° in the hole-meshed simulation (a) and the fine-mesh hole-modelled simulations with a uniform injection (b), a non-uniform injection (c), a turbulent uniform injection (d) and a turbulent non-uniform injection (e). The white dashed lined represents the mean streamline $\overline{\mathcal{S}}$ projected orthogonally onto the bottom boundary of the crossflow channel (refer to section 3.1.1 for details).

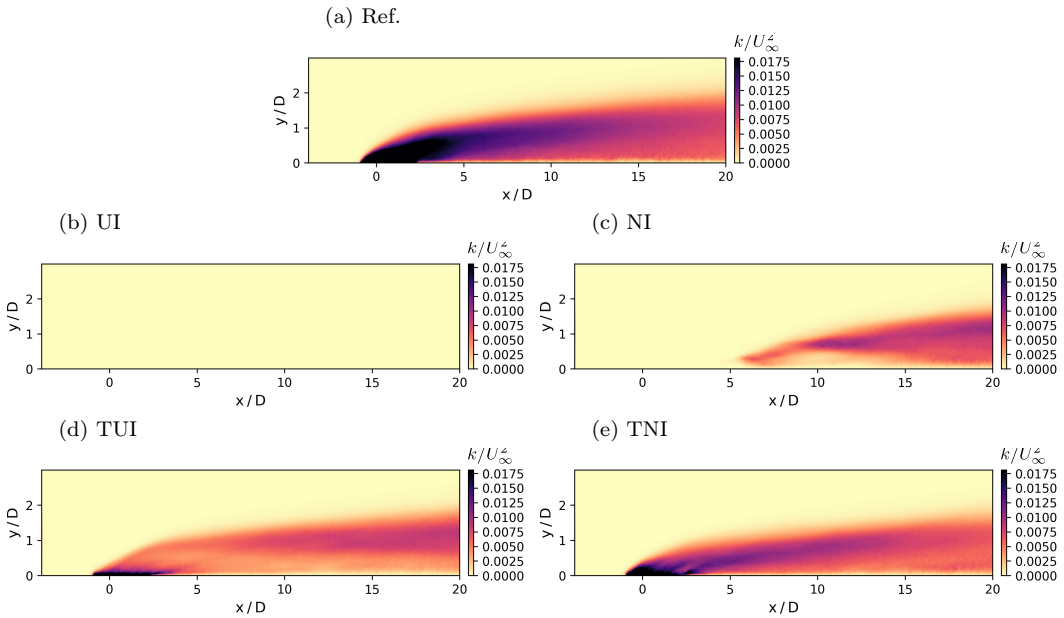

Figure 23: Mean turbulence kinetic energy on the centreline plane ($z = 0$) for the S&T777 hole at BR=1.5 without compound angle in the hole-meshed simulation (a) and the fine-mesh hole-modelled simulations with a uniform injection (b), a non-uniform injection (c), a turbulent uniform injection (d) and a turbulent non-uniform injection (e).

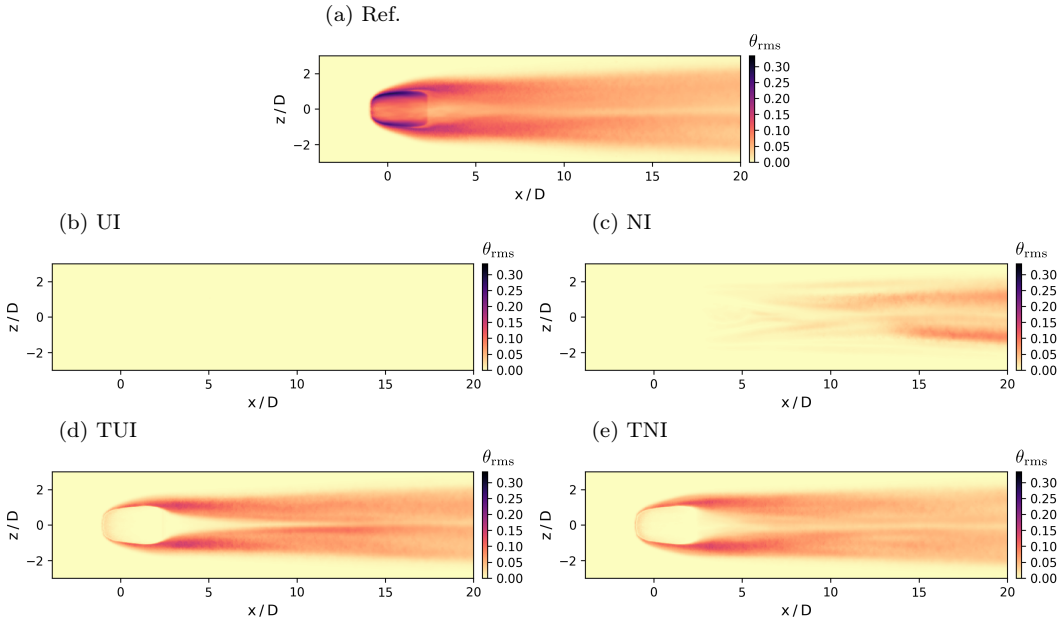

Figure 24: Standard deviation of adiabatic effectiveness on the plate ($y = 0$) for the S&T777 hole at BR=1.5 without compound angle in the hole-meshed simulation (a) and the fine-mesh hole-modelled simulations with a uniform injection (b), a non-uniform injection (c), a turbulent uniform injection (d) and a turbulent non-uniform injection (e).

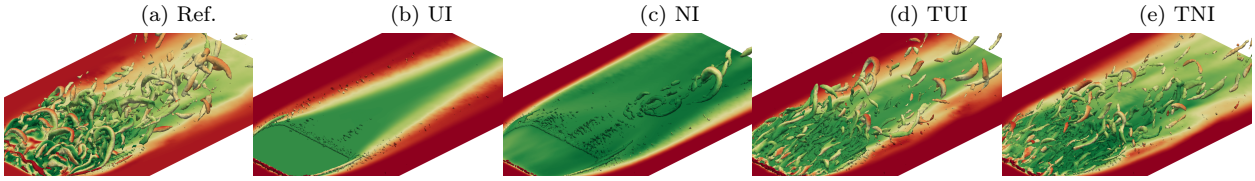

Figure 25: (Colour online) Instantaneous contour of Q criterion ($Q = 5.0 \times 10^6$ s^{-2}) around the hole exit for the GFS hole at BR=1.5 without compound angle in the hole-meshed simulation (a) and the fine-mesh hole-modelled simulations with a uniform injection (b), a non-uniform injection (c), a turbulent uniform injection (d) and a turbulent non-uniform injection (e). The surfaces are coloured by temperature, with green-coloured regions denoting colder fluid.

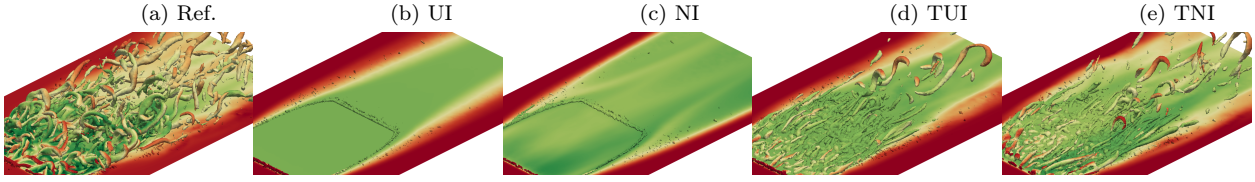

Figure 26: (Colour online) Instantaneous contour of Q criterion ($Q = 5.0 \times 10^6$ s^{-2}) around the hole exit for the GLBFS hole at BR=1.5 without compound angle in the hole-meshed simulation (a) and the fine-mesh hole-modelled simulations with a uniform injection (b), a non-uniform injection (c), a turbulent uniform injection (d) and a turbulent non-uniform injection (e). The surfaces are coloured by temperature, with green-coloured regions denoting colder fluid.

Table 5: Agreement between the hole-meshed simulations and the fine-mesh hole-modelled simulations for shaped holes. Refer to the caption of table 4 for notations.

Simulation			$\frac{\langle\langle T-T_{\mathrm{ref}}\rangle\rangle_{\mathcal{P}}}{\sqrt{\langle\langle T_{\mathrm{ref}}\rangle^2\rangle_{\mathcal{P}}}}$	$C_T^{\mathcal{P}}$	$C_{T'^2}^{\mathcal{P}}$	$C_T^{\mathcal{V}}$	$C_{\lvert\boldsymbol{U}\rvert}^{\mathcal{V}}$	$C_k^{\mathcal{V}}$	$d_{\overline{\mathcal{S}}}/D$	
GFS	BR=1.5 γ=0°	UI	0.30	0.630	-0.020	0.714	0.885	0.154	0.72	D*
GFS	BR=1.5 γ=0°	NI	0.70	0.530	-0.126	0.855	0.965	0.593	0.39	A
GFS	BR=1.5 γ=0°	TUI	0.12	0.845	0.511	0.927	0.966	0.882	0.51	A
GFS	BR=1.5 γ=0°	TNI	0.18	0.923	0.786	0.979	0.983	0.923	0.36	A
GLBFS	BR=1.5 γ=0°	UI	0.01	0.712	-0.001	0.707	0.899	0.002	0.64	D*
GLBFS	BR=1.5 γ=0°	NI	0.68	0.390	-0.001	0.745	0.922	0.003	0.49	A
GLBFS	BR=1.5 γ=0°	TUI	0.01	0.842	0.261	0.918	0.981	0.774	0.24	A
GLBFS	BR=1.5 γ=0°	TNI	0.18	0.912	0.420	0.953	0.992	0.820	0.31	A
S&T777	BR=1.5 γ=0°	UI	0.37	0.695	0.004	0.765	0.935	0.008	0.52	D*
S&T777	BR=1.5 γ=0°	NI	0.10	0.874	0.107	0.879	0.978	0.597	0.40	D*
S&T777	BR=1.5 γ=0°	TUI	0.09	0.960	0.851	0.976	0.988	0.858	0.30	A
S&T777	BR=1.5 γ=0°	TNI	0.11	0.971	0.848	0.982	0.993	0.893	0.06	A
S&T777	BR=1.5 γ=60°	UI	0.20	0.315	-0.132	0.634	0.892	0.376	0.84	A*
S&T777	BR=1.5 γ=60°	NI	0.05	0.750	0.231	0.855	0.964	0.571	0.30	D
S&T777	BR=1.5 γ=60°	TUI	0.11	0.650	0.429	0.763	0.921	0.619	0.69	D
S&T777	BR=1.5 γ=60°	TNI	0.01	0.965	0.811	0.987	0.993	0.962	0.36	D
S&T777	BR=3.0 γ=0°	UI	0.40	0.573	0.003	0.780	0.938	0.001	0.27	D*
S&T777	BR=3.0 γ=0°	NI	0.26	0.750	0.162	0.841	0.912	0.073	0.26	D*
S&T777	BR=3.0 γ=0°	TUI	0.21	0.884	0.778	0.959	0.963	0.609	0.22	A
S&T777	BR=3.0 γ=0°	TNI	0.02	0.991	0.901	0.985	0.989	0.917	0.13	A
S&T777	BR=2.5 γ=0°	UI	0.48	0.479	0.003	0.785	0.950	0.001	0.34	D*
S&T777	BR=2.5 γ=0°	NI	0.37	0.607	0.184	0.852	0.951	0.114	0.15	D*
S&T777	BR=2.5 γ=0°	TUI	0.22	0.878	0.834	0.962	0.974	0.633	0.20	A
S&T777	BR=2.5 γ=0°	TNI	0.01	0.988	0.897	0.983	0.991	0.897	0.17	A
S&T777	BR=2.0 γ=0°	UI	0.47	0.534	0.004	0.782	0.951	0.018	0.45	D*
S&T777	BR=2.0 γ=0°	NI	0.25	0.734	0.193	0.872	0.972	0.281	0.14	D*
S&T777	BR=2.0 γ=0°	TUI	0.18	0.920	0.869	0.969	0.982	0.701	0.26	A
S&T777	BR=2.0 γ=0°	TNI	0.05	0.983	0.863	0.982	0.992	0.871	0.19	A
S&T777	BR=1.0 γ=0°	UI	0.24	0.827	0.003	0.763	0.924	0.232	8.52	D*
S&T777	BR=1.0 γ=0°	NI	0.33	0.803	0.036	0.791	0.947	0.387	0.16	D*
S&T777	BR=1.0 γ=0°	TUI	0.06	0.960	0.718	0.980	0.993	0.939	0.14	A
S&T777	BR=1.0 γ=0°	TNI	0.12	0.958	0.719	0.979	0.994	0.926	0.24	A
S&T777	BR=0.5 γ=0°	UI	0.10	0.732	-0.048	0.738	0.947	0.419	0.21	D*
S&T777	BR=0.5 γ=0°	NI	0.59	0.602	-0.023	0.688	0.945	0.270	0.17	A
S&T777	BR=0.5 γ=0°	TUI	0.04	0.905	0.555	0.943	0.991	0.899	0.09	A
S&T777	BR=0.5 γ=0°	TNI	0.23	0.870	0.607	0.939	0.992	0.887	0.13	A
			0 0.5 1	0 0.5 1	0 0.5 1	0 0.5 1	0 0.5 1	0 0.5 1	0 0.5 1	

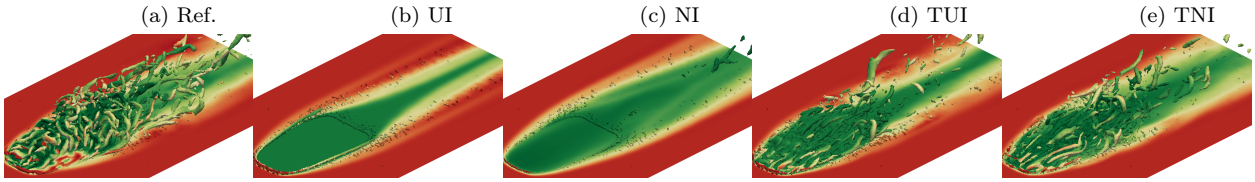

Figure 27: (Colour online) Instantaneous contour of Q criterion ($Q = 5.0\times10^6$ s^{-2}) around the hole exit for the S&T777 hole at BR=1.5 without compound angle in the hole-meshed simulation (a) and the fine-mesh hole-modelled simulations with a uniform injection (b), a non-uniform injection (c), a turbulent uniform injection (d) and a turbulent non-uniform injection (e). The surfaces are coloured by temperature, with green-coloured regions denoting colder fluid.

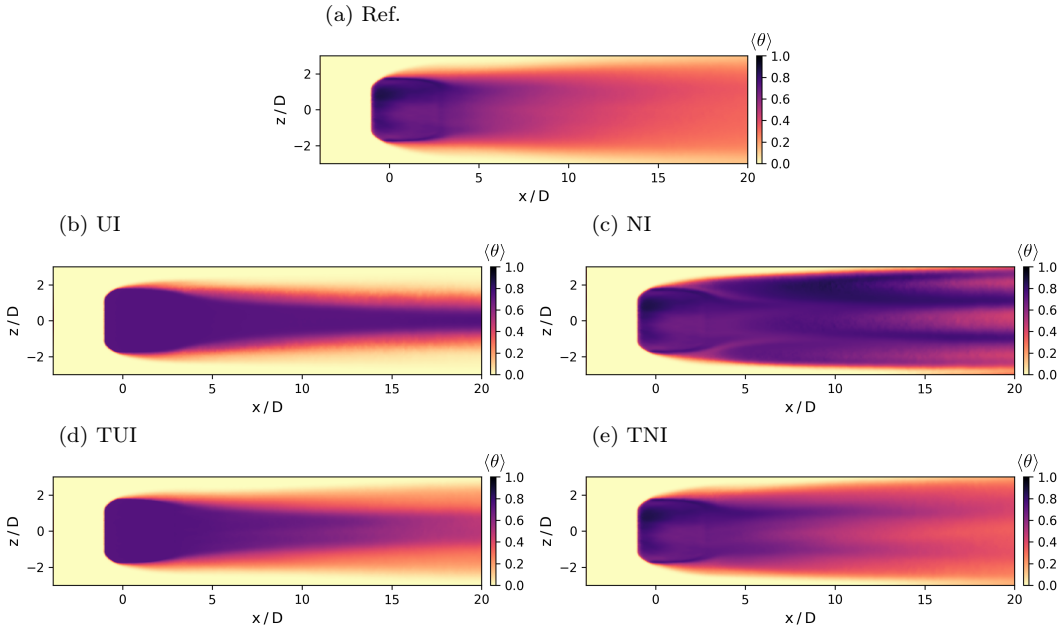

Figure 28: Mean adiabatic effectiveness on the plate ($y = 0$) for the GLBFS hole at BR=1.5 without compound angle in the hole-meshed simulation (a) and the fine-mesh hole-modelled simulations with a uniform injection (b), a non-uniform injection (c), a turbulent uniform injection (d) and a turbulent non-uniform injection (e).

in all investigated configurations judging from visual inspection and according to the concordance correlation coefficients reported in table 4 and 5. However, the mean adiabatic effectiveness on the plate, often the most important metric in practical applications, is not always improved in the turbulent non-uniform case as it is an integral measure sensitive to compensation of errors.

3.2 Effect of mesh refinement on the injection modelling predictions

This section compares the performance of hole-modelled simulations with a uniform, non-uniform, turbulent uniform and turbulent non-uniform injection using the coarse mesh presented in section 2.3. The primary objective of this comparison is to study the effect of a very coarse mesh resolution on the hole-model improvements. We thus selected a mesh sufficiently coarse not to capture accurately the flow dynamics, intended to be representative of a mesh that could be used for the numerical simulation of a complex geometry, such as a cooled nozzle guide vane.

As with the fine mesh, the performance of the hole-modelled simulations is compared to the results of the corresponding hole-meshed simulations. However, additional care should be taken while interpreting the results. First, the accuracy of the predictions strongly depends, given the large difference in mesh resolution, on the numerical method and the large-eddy simulation modelling hypotheses, both of which are outside the scope of this paper. For instance, the turbulent structures formed outside of the cooling hole cannot be captured by the simulation as they are smaller than the cell size near the hole. Their effect on the flow must therefore be accounted for by the subgrid-scale model. Second, the results of large-eddy simulations with different meshes can generally not be compared directly, since they are associated with two different large-eddy simulation filters. In order to evaluate the effect of the filtering, the hole-meshed simulation has been filtered at the resolution of the coarse-mesh simulations in the case S&T777 DR=1.5 γ=0°. To compute the filtered fields, the results were first interpolated on a uniform structured mesh of cell size $\Delta x = \Delta y = \Delta z = 0.026D$. A Gaussian filter corresponding to the characteristic length of the coarse-mesh cells is then applied, assuming local isotropy [42]. Finally, first- and second-order turbulence statistics are computed by averaging the results of 45 instantaneous fields, separated each by 0.064 flow-through time. The filtered mean velocity components and the filtered tempera-

Table 6: Agreement between the hole-meshed simulations and the coarse-mesh hole-modelled simulations. Refer to the caption of table 4 for notations.

Simulation	$\frac{\langle\langle T-T_{\mathrm{ref}}\rangle\rangle_{\mathcal{P}}}{\sqrt{\langle\langle T_{\mathrm{ref}}\rangle^2\rangle_{\mathcal{P}}}}$	$C_T^{\mathcal{P}}$	$C_{T'^2}^{\mathcal{P}}$	$C_T^{\mathcal{V}}$	$C_{\lvert U\rvert}^{\mathcal{V}}$	$C_k^{\mathcal{V}}$	$d_{\overline{S}}/D$	
Cylinder BR=1.5 γ=0° UI	0.40	0.560	0	0.864	0.912	0.004	1.20	D
Cylinder BR=1.5 γ=0° NI	0.55	0.231	0	0.785	0.903	0.010	0.92	D
Cylinder BR=1.5 γ=0° TUI	0.35	0.670	0.731	0.970	0.938	0.463	0.73	D
Cylinder BR=1.5 γ=0° TNI	0.45	0.349	0.808	0.947	0.938	0.743	0.73	D
Cylinder BR=0.5 γ=0° UI	0.39	0.670	0	0.866	0.917	0.020	0.62	D*
Cylinder BR=0.5 γ=0° NI	0.36	0.724	0	0.867	0.917	0.019	0.42	D*
Cylinder BR=0.5 γ=0° TUI	0.39	0.652	0.416	0.884	0.942	0.501	2.36	D*
Cylinder BR=0.5 γ=0° TNI	0.41	0.608	0.548	0.849	0.940	0.448	0.52	D*
Cylinder BR=0.5 γ=60° UI	0.48	0.347	-0.027	0.791	0.936	0.075	2.81	A
Cylinder BR=0.5 γ=60° NI	0.73	0.195	-0.017	0.755	0.933	0.015	3.02	D*
Cylinder BR=0.5 γ=60° TUI	0.43	0.377	-0.121	0.802	0.942	0.236	2.80	A
Cylinder BR=0.5 γ=60° TNI	0.66	0.211	-0.071	0.773	0.939	0.273	2.90	D*
GFS BR=1.5 γ=0° UI	0.34	0.676	-0.026	0.789	0.888	0.364	0.97	D*
GFS BR=1.5 γ=0° NI	0.24	0.739	-0.029	0.829	0.923	0.276	0.33	A
GFS BR=1.5 γ=0° TUI	0.23	0.760	0.192	0.896	0.940	0.700	0.75	A
GFS BR=1.5 γ=0° TNI	0.15	0.828	0.206	0.936	0.961	0.701	11.2	A
GLBFS BR=1.5 γ=0° UI	0.00	0.720	-0.079	0.761	0.894	0.100	0.74	A
GLBFS BR=1.5 γ=0° NI	0.55	0.557	-0.066	0.789	0.936	0.048	0.30	A
GLBFS BR=1.5 γ=0° TUI	0.02	0.814	0.157	0.910	0.961	0.678	0.57	A
GLBFS BR=1.5 γ=0° TNI	0.13	0.897	0.376	0.932	0.975	0.731	0.73	A
S&T777 BR=1.5 γ=0° UI	0.14	0.947	0.395	0.892	0.938	0.083	0.28	D*
S&T777 BR=1.5 γ=0° NI	0.22	0.904	0	0.882	0.929	0.010	0.34	D*
S&T777 BR=1.5 γ=0° TUI	0.23	0.903	0.697	0.940	0.941	0.528	0.43	D*
S&T777 BR=1.5 γ=0° TNI	0.23	0.904	0.765	0.948	0.954	0.650	0.25	D*
S&T777 BR=1.5 γ=60° UI	0.48	-0.097	0.017	0.681	0.879	0.025	2.05	A*
S&T777 BR=1.5 γ=60° NI	0.30	-0.041	-0.000	0.838	0.901	0.003	0.37	D
S&T777 BR=1.5 γ=60° TUI	0.34	-0.018	0.205	0.718	0.895	0.326	2.18	A*
S&T777 BR=1.5 γ=60° TNI	0.15	0.188	0.448	0.925	0.931	0.603	0.38	D
S&T777 BR=3.0 γ=0° UI	0.21	0.826	0.248	0.882	0.854	0.054	0.16	D*
S&T777 BR=3.0 γ=0° NI	0.41	0.616	0	0.872	0.805	0.001	0.48	D*
S&T777 BR=3.0 γ=0° TUI	0.25	0.830	0.862	0.947	0.875	0.260	0.28	D*
S&T777 BR=3.0 γ=0° TNI	0.24	0.825	0.849	0.966	0.922	0.658	0.35	D*
S&T777 BR=2.5 γ=0° UI	0.19	0.893	0.231	0.902	0.896	0.081	0.14	D*
S&T777 BR=2.5 γ=0° NI	0.39	0.656	0	0.894	0.841	0.003	0.54	D*
S&T777 BR=2.5 γ=0° TUI	0.24	0.860	0.837	0.946	0.900	0.285	0.23	D*
S&T777 BR=2.5 γ=0° TNI	0.27	0.833	0.856	0.973	0.928	0.627	0.21	D*
S&T777 BR=2.0 γ=0° UI	0.19	0.933	0.237	0.905	0.928	0.121	0.40	D*
S&T777 BR=2.0 γ=0° NI	0.30	0.832	0	0.902	0.897	0.007	0.40	D*
S&T777 BR=2.0 γ=0° TUI	0.24	0.893	0.734	0.945	0.926	0.363	0.39	D*
S&T777 BR=2.0 γ=0° TNI	0.24	0.904	0.797	0.970	0.940	0.611	0.25	D*
S&T777 BR=1.0 γ=0° UI	0.19	0.865	0.070	0.861	0.918	0.096	0.38	D*
S&T777 BR=1.0 γ=0° NI	0.15	0.818	0.332	0.821	0.940	0.133	0.18	A
S&T777 BR=1.0 γ=0° TUI	0.18	0.883	0.614	0.928	0.949	0.625	0.25	A
S&T777 BR=1.0 γ=0° TNI	0.02	0.892	0.680	0.889	0.954	0.521	0.16	A
S&T777 BR=0.5 γ=0° UI	0.01	0.814	0.007	0.816	0.912	0.019	0.52	A
S&T777 BR=0.5 γ=0° NI	0.28	0.728	0.134	0.760	0.927	0.094	0.32	A
S&T777 BR=0.5 γ=0° TUI	0.00	0.878	0.584	0.911	0.953	0.611	0.27	A
S&T777 BR=0.5 γ=0° TNI	0.18	0.803	0.596	0.838	0.950	0.485	0.22	A
	0 0.5 1	0 0.5 1	0 0.5 1	0 0.5 1	0 0.5 1	0 0.5 1	0 0.5 1	

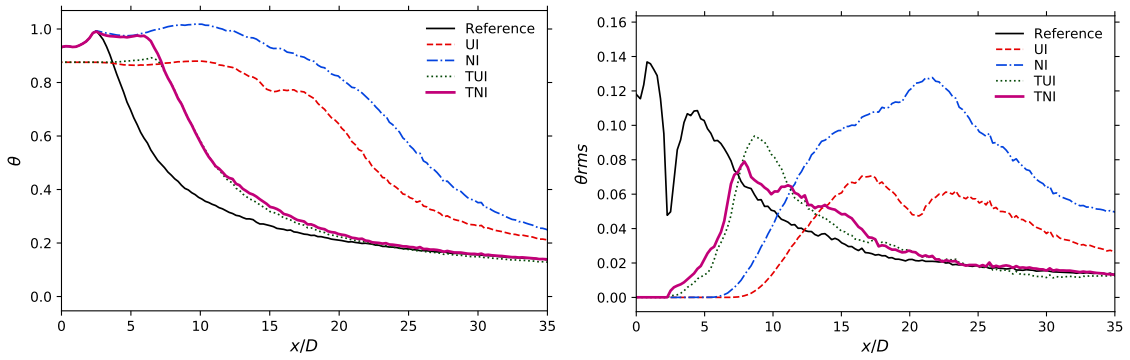

Figure 29: Centreline adiabatic effectiveness (left) and standard deviation of adiabatic effectiveness (right) for the S&T777 hole at BR=0.5 without compound angle in the hole-meshed simulation, the fine-mesh hole-modelled simulations with a uniform injection, a non-uniform injection, a turbulent uniform injection and a turbulent non-uniform injection.

ture are almost identical to their counterpart without filtering but second-order statistics are more sensitive to the filter application. In particular, the filtered turbulence kinetic energy is within the jet up to 30% lower than the turbulence kinetic energy without filtering (figure 30).

The results are summarised in table 6 using several global measures of the performance of the models. The concordance correlation coefficients suggest as expected that the quality of the predictions is lower with this very coarse mesh than with the fine mesh. The improvements provided by spatial inhomogeneity and turbulence injection to the hole model also seem more limited than for the fine mesh, in particular for the mean fields of velocity and temperature. This may be attributed to the fact that (a) the spatial inhomogeneity of the injection cannot be accurately represented with a coarse mesh; and (b) the synthetic turbulence injection is restricted to large scales while a large part of turbulence is associated with subgrid scales. Notable improvements are nevertheless observed in some configurations using a turbulent or non-uniform injection. For example, the predicted centreline adiabatic effectiveness is more accurate with a non-uniform injection than with a uniform injection with the GFS hole at BR=1.5 (figure 31), as the attachment of the jet to the wall is correctly described in those cases. Besides, the addition of synthetic turbulence injection increases the magnitude of all turbulence-related quantities downstream the hole, which are clearly underestimated with a non-turbulent injection. In particular, the resolved turbulence kinetic energy on the centreline plane is as shown by figure 32 improved if one uses a hole model with turbulent injection, but remains clearly underestimated, especially in the near-hole region. This underestimation of the turbulence intensity is more severe than in the fine-mesh simulations. As a result, the coarse-mesh hole-modelled simulations sometimes do not predict correctly the behaviour of the jet with the coarse mesh. With the S&T777 hole, the insufficient mixing of the jet within the crossflow results at a lower blowing ratio BR=0.5 in a large overestimation of the centreline adiabatic effectiveness (figure 33) while the vertical diffusion of the hot fluid and the lateral spreading of the thermal footprint are greatly underestimated (figure 34). By contrast, a large underestimation of the centreline adiabatic effectiveness is observed at a larger blowing ratio BR=2.5 (figure 35) as the lack of mixing results in the detachment of the jet from the wall (figure 36). With the fine mesh, the erroneous detachment of the jet occurred with a uniform injection, a non-uniform injection or a turbulent uniform injection but was corrected with the turbulent non-uniform hole model. With the coarse mesh, none of the hole-modelled simulations accurately predict the behaviour of the jet due to the additional deficit of mixing. This suggests that the subgrid-scale model used is not able to properly account for the effect of the subgrid turbulence structures in highly coarsened meshes, which was to be expected. In order to accurately predict the thermal footprint of the jet, hole-modelled large-eddy simulations thus require with the current modelling strategies a minimal level of mesh refinement within the jet, depending on the flow configuration or more deficiency aware modelling strategies.

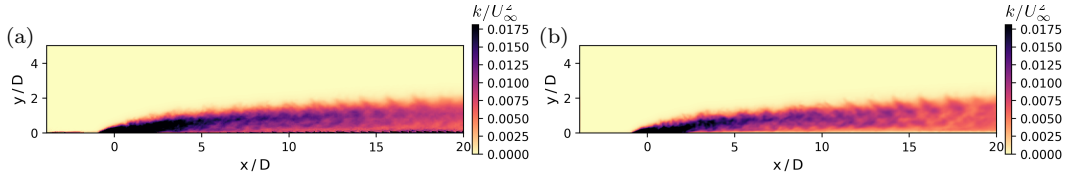

Figure 30: Mean turbulence kinetic energy on the centreline plane ($z = 0$) for the S&T777 hole at BR=1.5 without compound angle in the hole-meshed simulation without filtering (a) and filtered at the resolution of the coarse-mesh hole-modelled simulations (b).

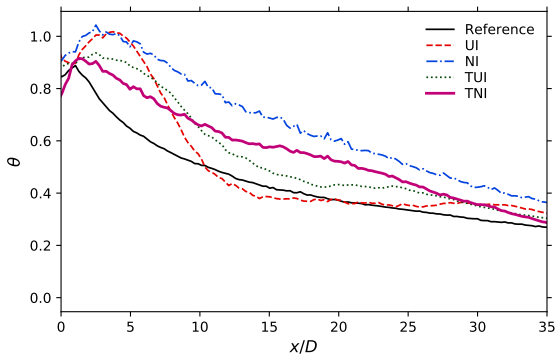

Figure 31: Centreline adiabatic effectiveness for the GFS hole at BR=1.5 without compound angle in the hole-meshed simulation, the coarse-mesh hole-modelled simulations with a uniform injection, a non-uniform injection, a turbulent uniform injection and a turbulent non-uniform injection.

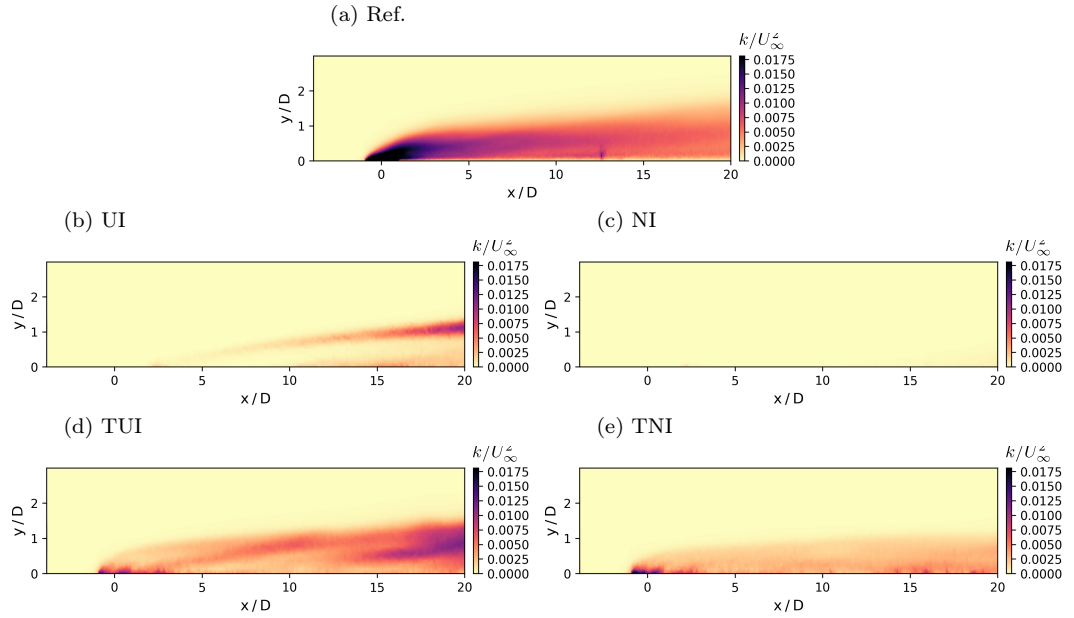

Figure 32: Mean resolved turbulence kinetic energy on the centreline plane ($z = 0$) for the GFS hole at BR=1.5 without compound angle in the hole-meshed simulation (a) and the coarse-mesh hole-modelled simulations with a uniform injection (b), a non-uniform injection (c), a turbulent uniform injection (d) and a turbulent non-uniform injection (e).

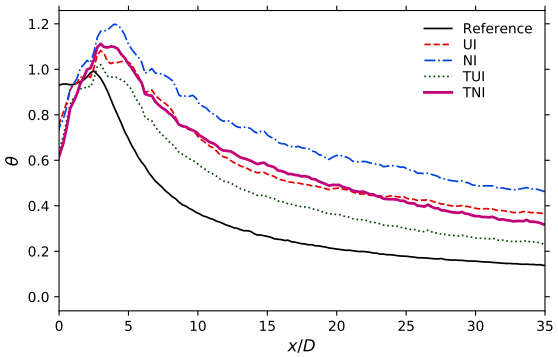

Figure 33: Centreline adiabatic effectiveness for the S&T777 hole at BR=0.5 without compound angle in the hole-meshed simulation, the coarse-mesh hole-modelled simulations with a uniform injection, a non-uniform injection, a turbulent uniform injection and a turbulent non-uniform injection.

4 Conclusion

Boundary-condition film-cooling hole models greatly reduce the computational resources required to simulate film-cooling systems by eliminating the need to mesh and simulate the in-hole flow. However, a basic injection model imposing a uniform velocity vector and temperature on the hole surface generally does not lead to satisfactory results as it greatly underestimates the turbulent mixing between the hot and cold fluid. To assess potential improvements to this baseline uniform model, namely taking into account the spatial inhomogeneity of the injection and adding synthetic turbulence to reproduce the in-hole agitation, 12 jet-in-crossflow configurations on a flat plate have been simulated without model and with four different hole models. A turbulent non-uniform injection provides significantly more accurate results than the baseline uniform model in all investigated configurations. In particular, the results of the hole-meshed and hole-modelled simulations are almost indistinguishable for a cylindrical hole. This suggest a lack of influence of the structures inside the hole as the eddies added are only necessary to trigger transition. For shaped holes, a lack of mixing and turbulence intensity is generally observed, leading to an overestimation of the cooling effectiveness. We suspect that this could be due to the presence of coherent structures inside the hole that are not reproduced by the hole model. With a very coarse mesh, a turbulent non-uniform injection also provides notable improvements compared to the baseline uniform model. However, an agreement between the hole-modelled simulations and the reference hole-meshed simulations is not obtained because of numerical and subgrid-scale modelling errors. The large-eddy simulation of industrial cooled high-pressure turbines thus requires a minimal level of mesh refinement around the holes with the current models. Future works could investigate the use of adaptive mesh refinement strategies to ensure a sufficient mesh resolution near the hole exit and provide quantitative mesh requirements. In addition, the injection of more realistic fluctuations could be assessed using a database obtained from hole-meshed simulations.

Acknowledgments

This work was granted access to the computer resources of CINES and TGCC under the allocation 2019-A0062A06074 made by GENCI. D. Dupuy has been funded by the RTRA-STAE foundation (Réseau thématique de recherche avancée Sciences et technologies pour l'aéronautique et l'espace).

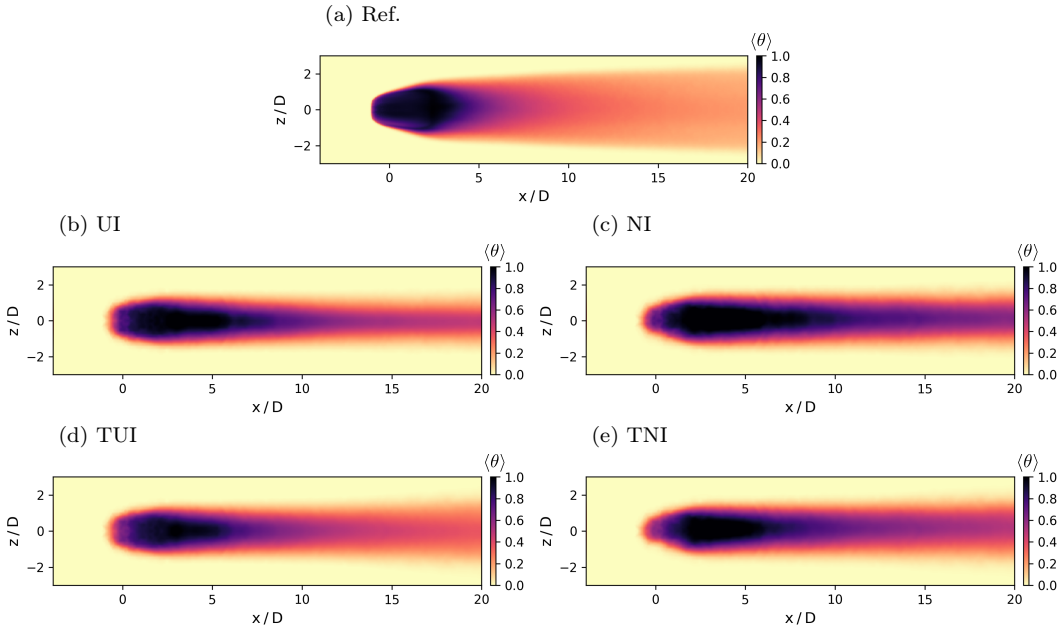

Figure 34: Mean adiabatic effectiveness on the plate ($y = 0$) for the S&T777 hole at BR=0.5 without compound angle in the hole-meshed simulation (a) and the coarse-mesh hole-modelled simulations with a uniform injection (b), a non-uniform injection (c), a turbulent uniform injection (d) and a turbulent non-uniform injection (e).

References

[1] S. Agarwal, L. Gicquel, F. Duchaine, N. Odier, J. Dombard, D. Bonneau, and M. Slusarz. Analysis of the unsteady flow field inside a fan-shaped cooling hole predicted by large-eddy simulation. In *ASME Turbo Expo 2020: Turbomachinery Technical Conference and Exposition*, number Accepted for publication. American Society of Mechanical Engineers, .

[2] S. Agarwal, L. Gicquel, F. Duchaine, N. Odier, J. Dombard, D. Bonneau, and M. Slusarz. Effect of the in-hole vortical structures on the cylindrical-hole film-cooling effectiveness. In *ASME Turbo Expo 2020: Turbomachinery Technical Conference and Exposition*, number Accepted for publication. American Society of Mechanical Engineers, .

[3] L. Andrei, L. Innocenti, A. Andreini, B. Facchini, and L. Winchler. Film cooling modeling for gas turbine nozzles and blades: Validation and application. *Journal of Turbomachinery*, 139(1), 2017.

[4] A. Andreini, R Da Soghe, B. Facchini, L. Mazzei, S. Colantuoni, and F. Turrini. Local source based CFD modeling of effusion cooling holes: Validation and application to an actual combustor test case. *Journal of engineering for gas turbines and power*, 136(1), 2014.

[5] T. auf dem Kampe and S. Völker. A model for cylindrical hole film cooling -— Part II: model formulation, implementation and results. pages 1541–1550, 2010.

[6] G. Bergeles, A. D. Gosman, and B. E. Launder. The near-field character of a jet discharged normal to a main stream. *Journal of Heat Transfer*, 98(3):373–378, 1976.

[7] G. Bergeles, A. D. Gosman, and B. E. Launder. Near-field character of a jet discharged through a wall at 30 deg toa mainstream. *AIAA journal*, 15(4):499–504, 1977.

[8] R. Bizzari, D. Lahbib, A. Dauptain, F. Duchaine, L. Gicquel, and F. Nicoud. A thickened-hole model for large eddy simulations over multiperforated liners. *Flow, Turbulence and Combustion*, 101(3): 705–717, 2018.

[9] D. G. Bogard and K. A. Thole. Gas turbine film cooling. *Journal of propulsion and power*, 22(2): 249–270, 2006.

[10] D. Brauckmann and J. von Wolfersdorf. Influence of compound angle on adiabatic film cooling effectiveness and heat transfer coefficient for a row of shaped film cooling holes. In *ASME Turbo Expo 2005: Power for Land, Sea, and Air*, pages 39–47. American Society of Mechanical Engineers Digital Collection, 2005.

[11] A. M. Briones, B. A. Rankin, S. D. Stouffer, T. J. Erdmann, and D. L. Burrus. Parallelized, automated,

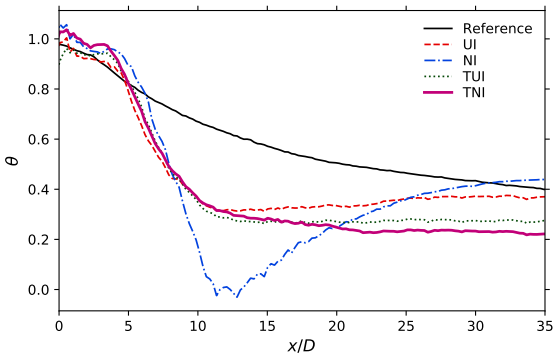

Figure 35: Centreline adiabatic effectiveness for the S&T777 hole at BR=2.5 without compound angle in the hole-meshed simulation, the coarse-mesh hole-modelled simulations with a uniform injection, a non-uniform injection, a turbulent uniform injection and a turbulent non-uniform injection.

and predictive imprint cooling model for combustion systems. *Journal of Engineering for Gas Turbines and Power*, 139(3), 2017.

[12] R. S. Bunker. A review of shaped hole turbine film-cooling technology. *Journal of Heat Transfer*, 127 (4):441–453, 2005.

[13] J. R. Cash and A. H. Karp. A variable order runge-kutta method for initial value problems with rapidly varying right-hand sides. *ACM Transactions on Mathematical Software (TOMS)*, 16(3):201–222, 1990.

[14] I. B. Celik, Z. N. Cehreli, and I. Yavuz. Index of resolution quality for large eddy simulations. *Journal of Fluids Engineering*, 127(5):949–958, 2005.

[15] O. Colin and M. Rudgyard. Development of high-order Taylor–Galerkin schemes for LES. *Journal of Computational Physics*, 162(2):338–371, 2000.

[16] G. Daviller, G. Oztarlik, and T. Poinsot. A generalized non-reflecting inlet boundary condition for steady and forced compressible flows with injection of vortical and acoustic waves. *Computers & Fluids*, 190:503–513, 2019.

[17] J. W. Deardorff. A numerical study of three-dimensional turbulent channel flow at large Reynolds numbers. *Journal of Fluid Mechanics*, 41(2):453–480, 1970.

[18] F. Duchaine, N. Maheu, V. Moureau, G. Balarac, and S. Moreau. Large-eddy simulation and conjugate heat transfer around a low-mach turbine blade. *Journal of Turbomachinery*, 136(5), 2014.

[19] E. R. G. Eckert and J. N. B. Livingood. *Comparison of effectiveness of convection-, transpiration-, and film-cooling methods with air as coolant*, volume 1182. National Advisory Committee for Aeronautics, 1954.

[20] H. Foroutan and S. Yavuzkurt. Numerical simulations of the near-field region of film cooling jets under high free stream turbulence: application of rans and hybrid urans/large eddy simulation models. *Journal of Heat Transfer*, 137(1), 2015.

[21] T. F. Fric and A. Roshko. Structure in the near field of the transverse jet. In *Turbulent Shear Flows 7*, pages 225–237. Springer, 1991.

[22] T. F. Fric and A. Roshko. Vortical structure in the wake of a transverse jet. *Journal of Fluid Mechanics*, 279:1–47, 1994.

[23] W.-S. Fu, W.-S. Chao, M. Tsubokura, C.-G. Li, and W.-H. Wang. Direct numerical simulation of film cooling with a fan-shaped hole under low Reynolds number conditions. *International Journal of Heat and Mass Transfer*, 123:544–560, 2018.

[24] L. Y. M. Gicquel, N. Gourdain, J.-F. Boussuge, H. Deniau, G. Staffelbach, P. Wolf, and T. Poinsot. High performance parallel computing of flows in complex geometries. *Comptes Rendus Mecanique*, 339(2-3):104–124, 2011.

[25] L. Y. M. Gicquel, G. Staffelbach, and T. Poinsot. Large eddy simulations of gaseous flames in gas turbine combustion chambers. *Progress in energy and combustion science*, 38(6):782–817, 2012.

[26] R. J. Goldstein. Film cooling. In *Advances in heat transfer*, volume 7, pages 321–379. Elsevier, 1971.

[27] M. Gritsch, A. Schulz, and S. Wittig. Adiabatic wall effectiveness measurements of film-cooling holes with expanded exits. *Journal of Turbomachinery*, 120(3):549–556, 1998.

[28] X. Guo, W. Schröder, and M. Meinke. Large-eddy simulations of film cooling flows. *Computers & Fluids*, 35(6):587–606, 2006.

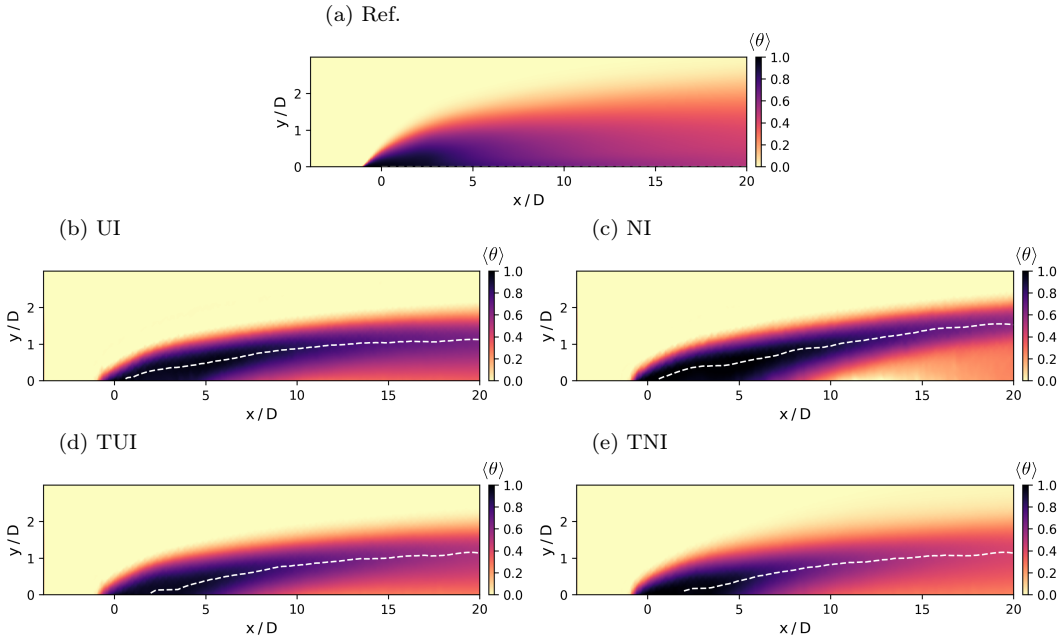

Figure 36: Mean nondimensionalised temperature on the centreline plane ($z = 0$) for the S&T777 hole at BR=2.5 without compound angle in the hole-meshed simulation (a) and the coarse-mesh hole-modelled simulations with a uniform injection (b), a non-uniform injection (c), a turbulent uniform injection (d) and a turbulent non-uniform injection (e). The white dashed line represents a ridgeline connecting local maxima of temperature.

[29] M. Harnieh, M. Thomas, R. Bizzari, J. Dombard, F. Duchaine, and L. Gicquel. Assessment of a coolant injection model on cooled high-pressure vanes with large-eddy simulation. *Flow, Turbulence and Combustion*, pages 1–30, 2019.

[30] S. Haydt and S. Lynch. Flowfield of a shaped film cooling hole over a range of compound angles. In *ASME Turbo Expo 2018: Turbomachinery Technical Conference and Exposition*. American Society of Mechanical Engineers Digital Collection, 2018.

[31] S. Haydt and S. Lynch. Cooling effectiveness for a shaped film cooling hole at a range of compound angles. *Journal of Turbomachinery*, 141(4), 2019.

[32] J. D. Heidmann and S. Ekkad. A novel anti-vortex turbine film cooling hole concept. In *ASME Turbo Expo 2007: Power for Land, Sea, and Air*, pages 487–496. American Society of Mechanical Engineers Digital Collection, 2007.

[33] A. Hoda and S. Acharya. Predictions of a film coolant jet in crossflow with different turbulence models. *Journal of Turbomachinery*, 122(3):558–569, 2000.

[34] P. L. Johnson and J. S. Kapat. Large-eddy simulations of a cylindrical film cooling hole. *Journal of thermophysics and heat transfer*, 27(2):255–273, 2013.

[35] R. M. Kelso and A. J. Smits. Horseshoe vortex systems resulting from the interaction between a laminar boundary layer and a transverse jet. *Physics of Fluids*, 7(1):153–158, 1995.

[36] R. M. Kelso, T. T. Lim, and A. E. Perry. An experimental study of round jets in cross-flow. *Journal of fluid mechanics*, 306:111–144, 1996.

[37] A. Kohli and K. A. Thole. A CFD investigation on the effects of entrance crossflow directions to film-cooling holes. *American Society of Mechanical Engineers, Heat Transfer Division,(Publication) HTD*, 350:223–232, 1997.

[38] R. H. Kraichnan. Diffusion by a random velocity field. *The physics of fluids*, 13(1):22–31, 1970.

[39] R. Krewinkel. A review of gas turbine effusion cooling studies. *International Journal of Heat and Mass Transfer*, 66:706–722, 2013.

[40] K. Kusterer, N. Tekin, F. Reiners, D. Bohn, T. Sugimoto, R. Tanaka, and M. Kazari. Highest-efficient film cooling by improved nekomimi film cooling holes: Part 1—ambient air flow conditions. In *ASME Turbo Expo 2013: Turbine Technical Conference and Exposition*. American Society of Mechanical Engineers Digital Collection, 2013.

[41] Karsten Kusterer, Dieter Bohn, Takao Sugimoto, and Ryozo Tanaka. Double-jet ejection of cooling air for improved film cooling. *Journal of Turbomachinery*, 129(4):809–815, 2007.

[42] A. Leonard. Energy cascade in large eddy simulations of turbulent fluid flows. *Advances in Geophysics*, 18A:237–248, 1974.

[43] W. Li, X. Li, J. Ren, and H. Jiang. Large eddy simulation of compound angle hole film cooling with hole length-to-diameter ratio and internal crossflow orientation effects. *International Journal of Thermal Sciences*, 121:410–423, 2017.

[44] C. H. Lim, G. Pullan, and P. Ireland. Influence of film cooling hole angles and geometries on aerodynamic loss and net heat flux reduction. *Journal of turbomachinery*, 135(5), 2013.

[45] L. I.-K. Lin. A concordance correlation coefficient to evaluate reproducibility. *Biometrics*, pages 255–268, 1989.

[46] K. Mahesh. The interaction of jets with crossflow. *Annual review of fluid mechanics*, 45:379–407, 2013.

[47] R. J. Margason. Fifty years of jet in cross flow research. In *Computational and Experimental Assessment of Jets in Cross Flow*. AGARD, 1993.

[48] K. T. McGovern and J. H. Leylek. A detailed analysis of film cooling physics: Part II—compound-angle injection with cylindrical holes. *Journal of Turbomachinery*, 122(1):113–121, 2000.

[49] S. Mendez and F. Nicoud. Adiabatic homogeneous model for flow around a multiperforated plate. *AIAA journal*, 46(10):2623–2633, 2008.

[50] F. Muldoon and S. Acharya. Direct numerical simulation of a film cooling jet. In *ASME Turbo Expo 2004: Power for Land, Sea, and Air*, pages 461–473. American Society of Mechanical Engineers Digital Collection, 2004.

[51] S. Muppidi and K. Mahesh. Direct numerical simulation of round turbulent jets in crossflow. *Journal of Fluid Mechanics*, 574:59–84, 2007.

[52] R.-H. Ni. A multiple grid scheme for solving the euler equations. In *5th Computational Fluid Dynamics Conference*, page 1025, 1981.

[53] F. Nicoud and F. Ducros. Subgrid-scale stress modelling based on the square of the velocity gradient tensor. *Flow, Turbulence and Combustion*, 62(3):183–200, 1999. ISSN 1386-6184.

[54] N. Odier, M. Sanjosé, L. Gicquel, T. Poinsot, S. Moreau, and F. Duchaine. A characteristic inlet boundary condition for compressible, turbulent, multispecies turbomachinery flows. *Computers & Fluids*, 178:41–55, 2019.

[55] T. A. Oliver, J. B. Anderson, D. G. Bogard, R. D. Moser, and G. Laskowski. Implicit LES for shaped-hole film cooling flow. In *ASME Turbo Expo 2017: Turbomachinery Technical Conference and Exposition*. American Society of Mechanical Engineers Digital Collection, 2017.

[56] T. A. Oliver, D. G. Bogard, and R. D. Moser. Large eddy simulation of compressible, shaped-hole film cooling. *International Journal of Heat and Mass Transfer*, 140:498–517, 2019.

[57] Y. V. Peet and S. K. Lele. Near field of film cooling jet issued into a flat plate boundary layer: LES study. In *ASME Turbo Expo 2008: Power for Land, Sea, and Air*, pages 409–418. American Society of Mechanical Engineers Digital Collection, 2008.

[58] T. J. Poinsot and S. K. Lele. Boundary conditions for direct simulations of compressible viscous flows. *Journal of computational physics*, 101(1):104–129, 1992.

[59] S. Rida, R. Reynolds, S. Chakravorty, and K. Gupta. Imprinted effusion modeling and dynamic CD calculation in gas turbine combustors. In *ASME Turbo Expo 2012: Turbine Technical Conference and Exposition*, pages 589–599. American Society of Mechanical Engineers Digital Collection, 2012.

[60] P. Sagaut. *Large eddy simulation for incompressible flows: an introduction*. Springer Science & Business Media, 2006.

[61] E. Sakai, T. Takahashi, and H. Watanabe. Large-eddy simulation of an inclined round jet issuing into a crossflow. *International Journal of Heat and Mass Transfer*, 69:300–311, 2014.

[62] J. E. Sargison, S. M. Guo, M. L. G. Oldfield, G. D. Lock, and A. J. Rawlinson. A converging slot-hole film-cooling geometry—part 1: low-speed flat-plate heat transfer and loss. *Journal of Turbomachinery*, 124(3):453–460, 2002.

[63] J. E. Sargison, S. M. Guo, M. L. G. Oldfield, G. D. Lock, and A. J. Rawlinson. A converging slot-hole film-cooling geometry—part 2: transonic nozzle guide vane heat transfer and loss. *Journal of Turbomachinery*, 124(3):461–471, 2002.

[64] D. L. Schmidt, B. Sen, and D. G. Bogard. Film cooling with compound angle holes: adiabatic effectiveness. *Journal of Turbomachinery*, 118(4):807–813, 1996.

[65] T. Schönfeld and M. Rudgyard. Steady and unsteady flow simulations using the hybrid flow solver AVBP. *AIAA journal*, 37(11):1378–1385, 1999.

[66] R. Schroeder and K. Thole. Adiabatic effectiveness measurements for a baseline shaped film cooling hole. In *ASME Turbo Expo*, pages GT2014–25992. American Society of Mechanical Engineers, 2014.

[67] B. Sen, D. L. Schmidt, and D. G. Bogard. Film cooling with compound angle holes: heat transfer. *Journal of Turbomachinery*, 118(4):800–806, 1996.

[68] M. Simon, S. Gautier, E. Vanoli, and P. Auzillon. Aerothermal simulations comparisons of a shaped-hole film cooling flow. In *ASME Turbo Expo 2019: Turbomachinery Technical Conference and Exposition*. American Society of Mechanical Engineers Digital Collection, 2019.

[69] S. H. Smith and M. G. Mungal. Mixing, structure and scaling of the jet in crossflow. *Journal of fluid mechanics*, 357:83–122, 1998.

[70] Z. T. Stratton and T. I.-P. Shih. Effects of density and blowing ratios on the turbulent structure and effectiveness of film cooling. *Journal of Turbomachinery*, 140(10), 2018.

[71] D. R. Stull and H. Prophet. Janaf thermochemical tables, 2nd edition. Technical Report NSRDS-NBS 37, US National Bureau of Standards, 1971.

[72] W. Sutherland. The viscosity of gases and molecular force. *The London, Edinburgh, and Dublin Philosophical Magazine and Journal of Science*, 36(223):507–531, 1893.

[73] K. Thole, W. Gritsch, A. Schulz, and S. Wittig. Flowfield measurements for film-cooling holes with expanded exits. *Journal of Turbomachinery*, 120(2):327–336, 1998.

[74] K. Tracy and S. P. Lynch. Large eddy simulation of the 7-7-7 shaped film cooling hole at axial and compound angle orientations. In *ASME Turbo Expo 2020: Turbomachinery Technical Conference and Exposition*, number Accepted for publication. American Society of Mechanical Engineers.

[75] M. Tyagi and S. Acharya. Large eddy simulation of film cooling flow from an inclined cylindrical jet. *Journal of Turbomachinery*, 125(4):734–742, 2003.

[76] S. Voigt, B. Noll, and M. Aigner. Development of a macroscopic CFD model for effusion cooling applications. In *ASME Turbo Expo 2012: Turbine Technical Conference and Exposition*, pages 1235–1243. American Society of Mechanical Engineers Digital Collection, 2012.

[77] C. Wang, J. Zhang, H. Feng, and Y. Huang. Large eddy simulation of film cooling flow from a fanshaped hole. *Applied Thermal Engineering*, 129:855–870, 2018.

[78] S. Yavuzkurt and M. Habte. Effect of computational grid on performance of two-equation models of turbulence for film cooling applications. In *ASME Turbo Expo 2008: Power for Land, Sea, and Air*, pages 133–143. American Society of Mechanical Engineers Digital Collection, 2008.

[79] S. Yavuzkurt and J. S. Hassan. Evaluation of two-equation models of turbulence in predicting film cooling performance under high free stream turbulence. In *ASME Turbo Expo 2007: Power for Land, Sea, and Air*, pages 259–268. American Society of Mechanical Engineers Digital Collection, 2007.

[80] L. Zhong, C. Zhou, and S. Chen. Large eddy simulation of inclined jet in cross flow with cylindrical and fan-shaped holes. In *ASME Turbo Expo 2016: Turbomachinery Technical Conference and Exposition*. American Society of Mechanical Engineers Digital Collection, 2016.